

PSR B0656+14: the unified outlook from the infrared to X-rays

S. Zharikov,¹* D. Zyuzin,² Yu. Shibano², A. Kirichenko,^{1,2} R. E. Mennickent,³ S. Geier,^{4,5}
A. Cabrera-Lavers^{4,5}

¹ Instituto de Astronomía, Universidad Nacional Autónoma de México, Apdo. Postal 877, Ensenada, Baja California, México, 22800

² Ioffe Institute, 26 Politekhnicheskaya st., St. Petersburg 194021, Russia

³ Departamento de Astronomía, Universidad de Concepción, Casilla 160-C, Concepción, Chile

⁴ Instituto de Astrofísica de Canarias, Vía Láctea s/n, E38200, La Laguna, Tenerife, Spain

⁵ GRANTECAN, Cuesta de San José s/n, E-38712, Breña Baja, La Palma, Spain

Accepted XXX. Received YYY; in original form ZZZ

ABSTRACT

We report detection of PSR B0656+14 with the Gran Telescopio Canarias in narrow optical $F657$, $F754$, $F802$, and $F902$ and near-infrared JHK_s bands. The pulsar detection in the K_s band extends its spectrum to $2.2\ \mu\text{m}$ and confirms its flux increase towards the infrared. We also present a thorough analysis of the optical spectrum obtained by us with the VLT. For a consistency check, we revised the pulsar near-infrared and narrow-band photometry obtained with the *HST*. We find no narrow spectral lines in the optical spectrum. We compile available near-infrared-optical-UV and archival 0.3–20 keV X-ray data and perform a self-consistent analysis of the rotation phase-integrated spectrum of the pulsar using unified spectral models. The spectrum is best fitted by the four-component model including two blackbodies, describing the thermal emission from the neutron star surface and its hot polar cap, the broken power-law, originating from the pulsar magnetosphere, and an absorption line near ~ 0.5 keV detected previously. The fit provides better constraints on the model parameters than using only a single spectral domain. The derived surface temperature is $T_{\text{NS}}^{\infty} = 7.9(3) \times 10^5$ K. The intrinsic radius (7.8–9.9 km) of the emitting region is smaller than a typical neutron star radius (13 km) and suggests a nonuniform temperature distribution over the star surface. In contrast, the derived radius of the hot polar cap is about twice as large as the ‘canonical’ one. The spectrum of the nonthermal emission steepens from the optical to X-rays and has a break near 0.1 keV. The X-ray data suggest the presence of another absorption line near 0.3 keV.

Key words: pulsars: general - pulsars, individual: PSR B0656+14 - stars: neutron

1 INTRODUCTION

More than fifty years after the discovery of the first neutron stars (NSs) as radio pulsars, their emission mechanisms still remain poorly understood, and multiwavelength observations are crucial for any progress in this field. Pulsars produce emission across the entire electromagnetic spectrum, being mostly observed as powerful radio, X-ray and γ -ray emitters. In contrast, their detection in the optical and/or near-infrared (near-IR) is still a rare event. The studies of most handful of them show that the optical emission consists of the thermal spectral component from the surface of the NS and the nonthermal component from its magnetosphere. Contribution of the components depends on the pulsar age. In turn, the near-IR emission is believed to have a purely magnetosphere nature.

The first optical and near-IR identifications of NSs have been reported shortly after the discovery of radio pulsars (Cocke et al. 1969) and to date number about 25 firm detections (see, e.g., Mignani (2011) for review). However, despite the rapidly increasing amount of known pulsars¹, no significant progress has been made in the field

during the last decade. Great expectations were set on the discoveries of the *Fermi* Large Area Telescope, which was launched in 2008 and has detected more than 200 γ -ray pulsars. Most of them appeared to be nearby and energetic, making them promising targets for optical and near-IR studies and boosting searches with the Hubble Space Telescope (*HST*) and the largest ground-based telescopes. However, among numerous optical and near-IR observations of γ -ray pulsars, only three possible identifications were proposed (Zyuzin et al. 2016, Mignani et al. 2016, Rangelov et al. 2017). Nevertheless, deep upper limits on the optical fluxes of other pulsars provided informative constraints on their emission properties and multiwavelength spectra (see, e.g., Zharikov & Mignani (2013), Mignani et al. (2018) and references therein).

Most of the identified NS optical counterparts are very faint ($V \geq 25$) and can be detected only via broad-band photometric observations. Optical spectroscopy has been obtained only for the youngest and brightest Crab pulsar (~ 1000 yr., $V = 16.6$) (Nasuti et al. 1996, Sollerman et al. 2000, Beskin & Neustroev 2001), PSR B0540–69 (~ 2000 yr., $V = 22.4$) (Hill et al. 1997, Serafimovich et al. 2004) and the third optically brightest Vela pulsar (~ 10000 yr., $V = 23.6$) (Mignani et al. 2007). The spectroscopic observations of older and fainter pulsars were first obtained by Martin et al. (1998). They re-

* E-mail: zhar@astro.unam.mx

¹ <http://www.atnf.csiro.au/people/pulsar/psrcat/>, Manchester et al. (2005)

ported observations of the Geminga pulsar ($\sim 3 \times 10^5$ yr, $R = 25.5$) using the Keck telescope. The preliminary optical spectroscopy for another middle-aged PSR B0656+14 ($\sim 10^5$ yr, $R = 24.6$) was reported by Zharikov et al. (2007). In addition, spectroscopic observations of the isolated radio-silent neutron star (INS) RX J1856.5-3754 ($\sim 5 \times 10^5$ yr, $V = 25.6$) were performed with the Very Large Telescope (VLT) by van Kerkwijk & Kulkarni (2001). The young Crab, Vela, and middle-aged Geminga pulsars demonstrate an almost a flat spectrum in the optical and near-IR (Sandberg & Sollerman 2009, Shibano et al. 2006, Zyuzin et al. 2013). In contrast, young B0540-69 (Mignani et al. 2019) and the middle-aged B0656+14 (Shibano et al. 2006) exhibit a flux increase towards the near-IR. Moreover, the optical-IR data of B0656+14 suggests the presence of a spectral break between the two ranges. Thorough studies in the near-IR are crucial to broaden the distribution and reveal the presence of similar features in other objects, which is important for understanding the physics of emitting particles in pulsar magnetospheres.

Owing to its relative brightness and proximity, the middle-aged PSR B0656+14 is one of those isolated NSs most intensively studied in different wavelengths. It was first discovered as a radio pulsar by Manchester et al. (1978). The average pulse flux densities of the pulsar, 6.5(6), 3.8(6), 4.8(1.4) and 3.7(8) mJy at 0.4, 0.6, 0.9 and 1.4 GHz, respectively, result in a power-law (PL) spectrum $S \sim \nu^{-\alpha}$ with the index $\alpha = 0.5(2)$ (Lorimer et al. 1995). The PSR B0656+14 pulse profile is almost completely linearly polarised with a shallow asymmetric swing of the position angle (Gould & Lyne 1998). Kuzmin & Ershov (2006) suggested and Weltevrede et al. (2006) and Tao et al. (2012) confirmed that PSR B0656+14 belongs to the group of pulsars that emit giant pulses with the peak flux density of the strongest pulse by a factor of 630 higher than of the average pulse. The pulsar dispersion measure is $13.977 \text{ pc cm}^{-3}$. Briskin et al. (2003) measured the parallax $\pi = 3.47(36)$ mas with the Very Long Baseline Array yielding a distance of 288^{+33}_{-27} pc. PSR B0656+14 is located near the centre of the Monogem ring (Nousek et al. 1981), a $\sim 10^5$ yr expanding supernova remnant (SNR) likely produced in the same supernova explosion as the pulsar (Thorsett et al. 2003). The basic parameters of PSR B0656+14 inferred from the radio observations are given in Table 1.

The pulsar has been detected and intensively studied in X-rays with the space observatories *Einstein* (Cordova et al. 1989), *ROSAT* (Finley et al. 1992, Anderson et al. 1993, Possenti et al. 1996), *ASCA* (Greiveldinger et al. 1996), *BeppoSAX* (Mineo et al. 2002), *XMM-Newton* (Zavlin & Pavlov 2004, De Luca et al. 2005), *Chandra* (Marshall & Schulz 2002, Pavlov et al. 2002, Lloyd et al. 2003, Birzan et al. 2016) and *NuSTAR* (Arumugasamy et al. 2018). It has also been observed with *SRG/eROSITA* during the verification stage at the end of 2019². The observed flux in the 0.2-3.0 keV band is about $1.01(3) \times 10^{-11} \text{ ergs cm}^{-2} \text{ s}^{-1}$. The observed X-ray spectrum consists of at least two distinct components, thermal and non-thermal. It appeared to be best fitted by an absorbed blackbody (BB) model with a relatively low temperature $T \approx (6 - 7) \times 10^5 \text{ K}$ combined with the additional BB with a higher temperature of $\approx 1.3 \times 10^6 \text{ K}$ and the PL describing the hard X-ray tail (De Luca et al. 2005). The non-thermal PL component of the pulsar magnetosphere origin contributes only 1% of the total luminosity in the 0.1-10 keV range. The low temperature BB component represents the thermal emission from the bulk of the surface of the NS, while the hot BB component is from its small polar

caps heated by relativistic particles from the magnetosphere of the pulsar. A historical summary of the X-ray spectral fits including the *EUVE* Deep Survey (DS) data (Edelstein et al. 2000) is presented in Fig. 1 and Table 2. The temperature of the bulk surface of the pulsar provided by the cold BB component despite of a noticeable uncertainty is consistent with prediction of cooling scenarios of NSs (Beznogov & Yakovlev 2015). However, the 2BB+PL model gives a strong scatter in the absorbing column density $N_H = (1.5-5.5) \times 10^{20} \text{ cm}^{-2}$. The X-ray observations also showed a complex behavior of the source pulsed fraction: it decreases with energy from about 20% at $\sim 0.1-0.3 \text{ keV}$ down to about 7-11% at around 1 keV and increases again to $\approx 35-44\%$ at $\geq 1 \text{ keV}$ (Pavlov et al. 2002, Lloyd et al. 2003, De Luca et al. 2005). Recently, Arumugasamy et al. (2018) reported the spectral analysis of new data obtained with *XMM-Newton* and *NuSTAR*. They found that the 2BB+PL model is not consistent with the new data due to large fit-residuals in the 0.3-0.7 keV range. However, the residuals can be naturally explained by the presence of an absorption line in the spectrum of the pulsar. The latter has been confirmed at a higher confidence by the recent *SRG/eROSITA* data (Schwope et al. 2019). Using NS atmosphere models, such as *NSA* (Zavlin et al. 1996) and *NSMAXG* (Ho 2014), does not lead to acceptable fits either.

Ramanamurthy et al. (1996) reported detection of PSR B0656+14 in γ -rays with the *EGRET* telescope aboard the Compton Gamma Ray Observatory. They found that the phase-averaged high-energy γ -ray pulsed emission from the pulsar has a single power-law (PL) spectrum with the photon index $\Gamma = 2.8(3)$ and the integral flux $4.1(1.4) \times 10^{-8} \text{ photons cm}^{-2} \text{ s}^{-1}$ above 100 MeV. This was confirmed by the *Fermi* Large Area Telescope (LAT) (Abdo et al. 2013). The pulsar was detected with a pulsed flux of $7.1(6) \times 10^{-8} \text{ photons cm}^{-2} \text{ s}^{-1}$ and a photon index of $\Gamma = 2.83(3)$ for the PL and $\Gamma = 1.35(13)$ for the PLEC³ spectral models, respectively, corresponding to the energy flux $2.7(1) \times 10^{-11} \text{ ergs cm}^{-2} \text{ s}^{-1}$ in the 100 MeV to 100 GeV range (Abdollahi et al. 2020).

The optical counterpart of PSR B0656+14 ($V \sim 25$) was discovered by Caraveo et al. (1994) and confirmed by Pavlov et al. (1996), Kurt et al. (1997) and Shearer et al. (1997). Later, Kurt et al. (1998) reported the first *BVRI* photometric observations of the PSR B0656+14 optical counterpart, which showed that the pulsar optical radiation has a non-thermal origin. The optical investigations were extended using the *HST* and the largest ground-based telescopes, such as the VLT. They afforded an opportunity to perform time-resolved photometry, to compile the detailed UV-optical-IR spectral energy distribution and to measure the phase-averaged and phase-resolved linear polarisation (Mignani et al. 2000, Koptsevich et al. 2001, Kern et al. 2003, Shibano et al. 2005, 2006, Zharikov et al. 2007, Durant et al. 2011, Mignani et al. 2015).

The total galactic interstellar colour excess $E(B - V)$ towards PSR B0656+14 obtained using the *COBE* and *IRAS* data is 0.09 (Schlegel et al. 1998). Based on analyses of hydrogen column densities from the radio and X-ray observations, Shibano et al. (2006) concluded that the most likely value of the colour excess in the pulsar direction is $E(B - V) = 0.03$. The new 3D interstellar dust reddening model⁴ (Green et al. 2015, 2018), gives a total $E(B - V)$ of 0.06 and, together with the pulsar parallax distance of 0.288 kpc, yields the colour excess towards PSR B0656+14 of $E(B - V) = 0.01^{+0.02}_{-0.01}$. Therefore, in the following analyses, we consider the in-

³ Power law Super Exponential Cutoff model (Abdo et al. 2013)

⁴ <http://argonaut.skymaps.info>: it is based on analyses of Pan-STARRS 1 and 2MASS stellar photometry

² <http://www.mpe.mpg.de/7362694/presskit-erosita-firstlight>

Table 1. Parameters of PSR B0656+14 obtained from radio observations (Taylor et al. 1993). The pulsar proper motion and distance are adopted from Briskin et al. (2003).

Observed								Derived		
P	\dot{P}	DM	l	b	μ_α	μ_δ	d	τ	B	\dot{E}
ms	10^{-14}	$\text{cm}^{-3} \text{ pc}$	deg	deg	mas yr^{-1}	mas yr^{-1}	pc	Myr	G	erg s^{-1}
384.87	5.50	13.977	201.1	8.3	44.07 ± 0.63	$-2.40 \pm .29$	288^{+33}_{-27}	0.11	4.7×10^{12}	3.8×10^{34}

P - spin period; \dot{P} - derivative of the spin period; DM - the dispersion measure; l, b - Galactic coordinate; μ_α, μ_δ - proper motion; d - distance; τ - the pulsar age; B - magnetic field strength; \dot{E} - spin-down luminosity

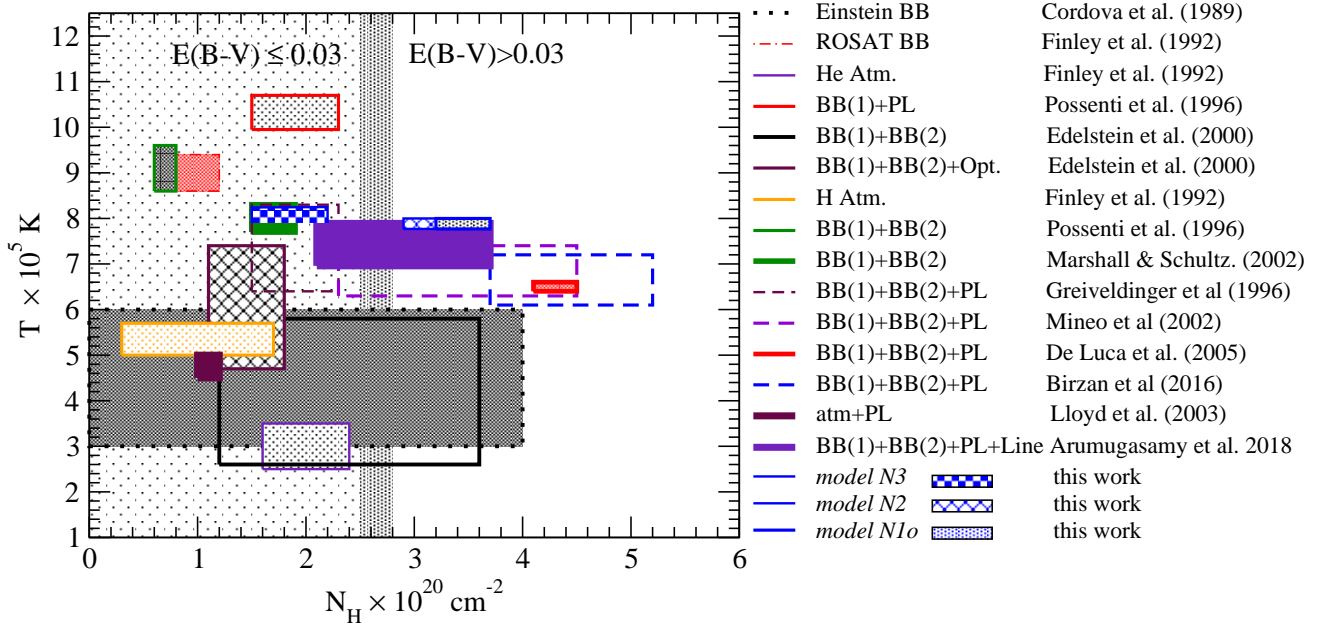


Figure 1. Diagram of the surface temperature T of the NS vs the absorbing column density N_H towards the pulsar. These are compiled results of various spectral fits of PSR B0656+14 X-ray emission published by different authors listed in the legend. In the legend, BB(1) is the low-temperature blackbody spectral component from the bulk of the NS surface, BB(2) is the high-temperature blackbody component from the hot polar spots of the pulsar and PL corresponds to the nonthermal component originating from the pulsar magnetosphere. Boxes show various 1σ constraints on the BB(1) temperature and N_H taken from the publications (see Table 2). The result of this work is also announced. The most plausible for the pulsar colour-excess range $E(B - V) \leq 0.03$ is shown by the short-dash-hatched region (see text for details).

terstellar absorption in the pulsar direction $E(B - V) \leq 0.03$. The low total galactic absorption and the small colour excess of the pulsar flux allow us to apply the dependence $N_H = 8.3 \times 10^{21} \text{ cm}^{-2} \times E(B - V)$ (Liszt 2014) to estimate the hydrogen column density towards the pulsar of $N_H \lesssim 2.5 \times 10^{20} \text{ cm}^{-2}$. Another estimation of hydrogen column density towards the pulsar is based on the empirical relation between the hydrogen column density and optical extinction obtained by Foight et al. (2016) using the *Chandra* SNR archive. They found the empirical relation $N_H = 2.87 \pm 0.12 \times 10^{21} A_V$ which gives $N_H \lesssim 2.8 \times 10^{20} \text{ cm}^{-2}$ to the pulsar using the standard reddening $A_V = 3.2E(B - V)$ law. This N_H constraint shown by the dash-hatched region in Fig.1 can be used in spectral analyses of the multi-wavelength data from the near-IR through X-rays. First attempts of such analysis for PSR B0656+14 were undertaken by Edelstein et al. (2000) and Lloyd et al. (2003) using a very limited set of data available at that time. This approach was shown to be potentially useful for obtaining tighter constraints on the pulsar parameters as compared to those inferred from separate spectral ranges. Given a considerable amount of new near-IR-optical-UV and X-ray

data obtained since that time, it is useful to repeat such analysis using a modern approach.

In this paper we focus on such multi-wavelength data analysis for this pulsar. We include our new optical narrow-band and near-IR *JHK* band photometric observations obtained with the Gran Telescopio Canarias (GTC). We also present a detailed analysis of our VLT spectroscopic medium resolution observations of the pulsar whose preliminary results were only shortly reported in Zharikov et al. (2007). For a consistent comparison with the VLT spectral and GTC photometric data we revised the pulsar narrow-band optical and broad-band near-IR data obtained with the HST and presented by Durant et al. (2011). We show that hints of the optical absorption/emission features in the spectrum of the pulsar reported by these authors are insignificant. We extracted X-ray data from different missions from archives, including the recently obtained but not yet published *XMM-Newton* data, that double the number of the pulsar source counts in soft X-rays. We re-reduced the data with modern versions of the respective tools, and used them to search for a common spectral solution across the IR-Optical-UV-X-ray do-

Table 2. Summary of X-ray spectral analyses of PSR B0656+14 published during the period 1989–2018.

Satellite	Range keV	Models (1)-soft; (2)-hard	Temperature/spec. index $\times 10^5$ K / $F \propto \nu^\alpha \propto \nu^{-\Gamma+1}$	N_H cm^{-2}	Reference
<i>Einstein</i>	0.15 — 4.0 keV	single BB(1);	$T_1 = 3.0\text{--}6.0$	$< 4 \times 10^{20}$	Cordova et al. (1989)
	0.15 — 4.0 keV	PL			
<i>ROSAT</i>	0.1 — 2.4 keV	single BB(1)	$T_1 = 8.6\text{--}9.4$	$(0.8\text{--}1.2) \times 10^{20}$	Finley et al. (1992)
	0.1 — 2.4 keV	PL	$\alpha_{PL} = -4.8$	$(0.8\text{--}1.2) \times 10^{20}$	
	0.1 — 2.4 keV	He Atm.	$T_1 = 2.5\text{--}3.5$	$(1.6\text{--}2.4) \times 10^{20}$	
	0.1 — 2.4 keV	H Atm.	$T_1 = 5.0\text{--}5.7$	$(0.3\text{--}1.7) \times 10^{20}$	Anderson et al. (1993)
	0.1 — 2.4 keV	BB(1)+BB(2)	$T_1 = 8.6\text{--}9.6$	$(0.6\text{--}0.8) \times 10^{20}$	Possenti et al. (1996)
			$T_2 = 15\text{--}23$		
	0.1 — 2.4 keV	BB(1)+PL	$T_1 = 9.95\text{--}1.07$	$(1.5\text{--}2.3) \times 10^{20}$	Possenti et al. (1996)
			$\alpha_{PL} = -3.4(4)$		
<i>ASCA</i>	0.5 — 10.0 keV	BB(1)+BB(2)+PL	$T_1 = 6.4\text{--}8.3$	$(1.5\text{--}2.3) \times 10^{20}$	Greiveldinger et al. (1996)
			$T_2 = 13\text{--}17$		
			$\alpha_{PL} = -0.5(1.1)$		
<i>BeppoSAX</i>	0.1 — 10.0 keV	BB(1)+BB(2)+PL	$T_1 = 6.3\text{--}7.4$	$(2.3\text{--}4.5) \times 10^{20}$	Mineo et al. (2002)
			$T_2 = 13\text{--}15$		
			$\alpha_{PL} = -1.08(41)$		
<i>Chandra</i>	0.1 — 2.0 keV	BB(1)+BB(2)	$T_1 = 7.7\text{--}8.3$	$(1.5\text{--}1.9) \times 10^{20}$	Marshall & Schulz (2002)
			$T_2 = 13\text{--}19$		
<i>Chandra</i>	0.3 — 8.0 keV	BB(1)+BB(2)+PL	$T_1 = 6.1\text{--}7.2$	$(3.7\text{--}5.2) \times 10^{20}$	Bîrzan et al. (2016)
			$T_2 = 12.1\text{--}13.6$		
			$\alpha_{PL} = -1.3(7)$		
<i>XMM-Newton</i>	0.1 — 10.0 keV	BB(1)+BB(2)+PL	$T_1 = 6.4\text{--}6.6$	$(4.1\text{--}4.5) \times 10^{20}$	De Luca et al. (2005)
			$T_2 = 12.2\text{--}12.8$		
			$\alpha_{PL} = -1.1(3)$		
<i>EUVE + ROSAT</i>	0.1 — 2.4 keV	BB(1)+BB(2)	$T_1 = 2.6\text{--}5.8$	$(1.2\text{--}3.6) \times 10^{20}$	Edelstein et al. (2000)
			$T_2 = 10.6\text{--}12.8$		
<i>EUVE + ROSAT</i> + Optical	0.1 — 2.4 keV	BB(1)+BB(2)	$T_1 = 4.7\text{--}7.4$	$(1.1\text{--}1.8) \times 10^{20}$	Edelstein et al. (2000)
			$T_2 = 11\text{--}18$		
<i>Chandra + Optical</i>	0.3 — 6 keV	H Atm. + PL	$T = 4.8\text{--}6.2$	$(1.0\text{--}1.2) \times 10^{20}$	Lloyd et al. (2003)
			$T^\infty = 4.5\text{--}5$		
			$\alpha_{PL} = -0.5$		
<i>XMM + NuStar</i>	0.3 — 7.0 keV	BB(1)+BB(2)+PL+Line	$T = 6.8\text{--}7.9$	$(2.1\text{--}3.7) \times 10^{20}$	Arumugasamy et al. (2018)
			$\alpha_{PL} = -0.7(1)$		(A18)

Comments: BB(1) is the blackbody from the NS surface; BB(2) – blackbody from its hot spot; PL – power law component; He Atm – He atmosphere model; H Atm – H-atmosphere model.

mains. The details of new GTC observations and data analysis are described in Section 2, clarification of the *HST* near-IR photometric results using the GTC data is presented in Section 3, analyses of the VLT spectroscopy and reanalysis of the *HST* optical narrow-band photometric data are given in Sections 4 and 5. The X-ray data are described in Section 6. The results and discussion are presented in Sections 7, 8 and conclusions in Section 9.

2 THE GTC DATA

2.1 Optical narrow-band imaging

The narrow-band photometric observations of PSR B0656+14 were obtained using the Optical System for Imaging and low-intermediate Resolution Integrated Spectroscopy (OSIRIS⁵) in the *F657/35*, *F754/50*, *F802/51* and *F902/44* narrow bands⁶ during several runs in 2009–2012⁷. The instrument contains two CCDs with a plate scale

of 0.254 arcsec/pixel (2×2 binning) and a total field of view (FoV) of 7'8×7'8. The log of observations is given in Table 3.

Standard data reduction, including bias subtraction, flat-fielding and cosmic-ray removal, was applied to the raw data using *ESO-MIDAS* routines⁸. Some of the resulting images appeared to have detector defects in the pulsar location, and for this reason were rejected. The total integration time for the resulting summed images was 2.1, 2.4, 3.6 and 15.775 ks for the *F657/35*, *F754/50*, *F802/51* and *F902/44* bands, respectively. The images were astrometrically calibrated using the *IRAF ccmmap* task and a set of eight reference stars in the vicinity of the pulsar from the *GAIA* catalog ([Gaia Collaboration et al. 2016, 2018](#)). The *rms* error of the calibrations was $\approx 0''.05$ in both directions. Selections of another sets of nearby *GAIA* stars did not affect this result significantly. For the photometric calibration, spectrophotometric standard stars He3, G191-B2B and Feige34 ([Oke 1974](#), [Stone 1977](#), [Massey et al. 1988](#), [Oke 1990](#)) were observed each observing night in the corresponding bands (see Table 3) and respective magnitude zero-points were obtained.

The resulting images are presented in Fig. 2. The pulsar optical counterpart is clearly detected on the combined images in all the

⁵ see <http://www.gtc.iac.es/instruments/osiris/> for details

⁶ The band pivot wavelengths and widths in nm units are the first and second numbers in filter ID names.

⁷ Proposals GTC4-09BCATMEX and GTC1-11BIACMEX, PI S. Zharikov

⁸ <https://www.eso.org/sci/software/esomidas/>

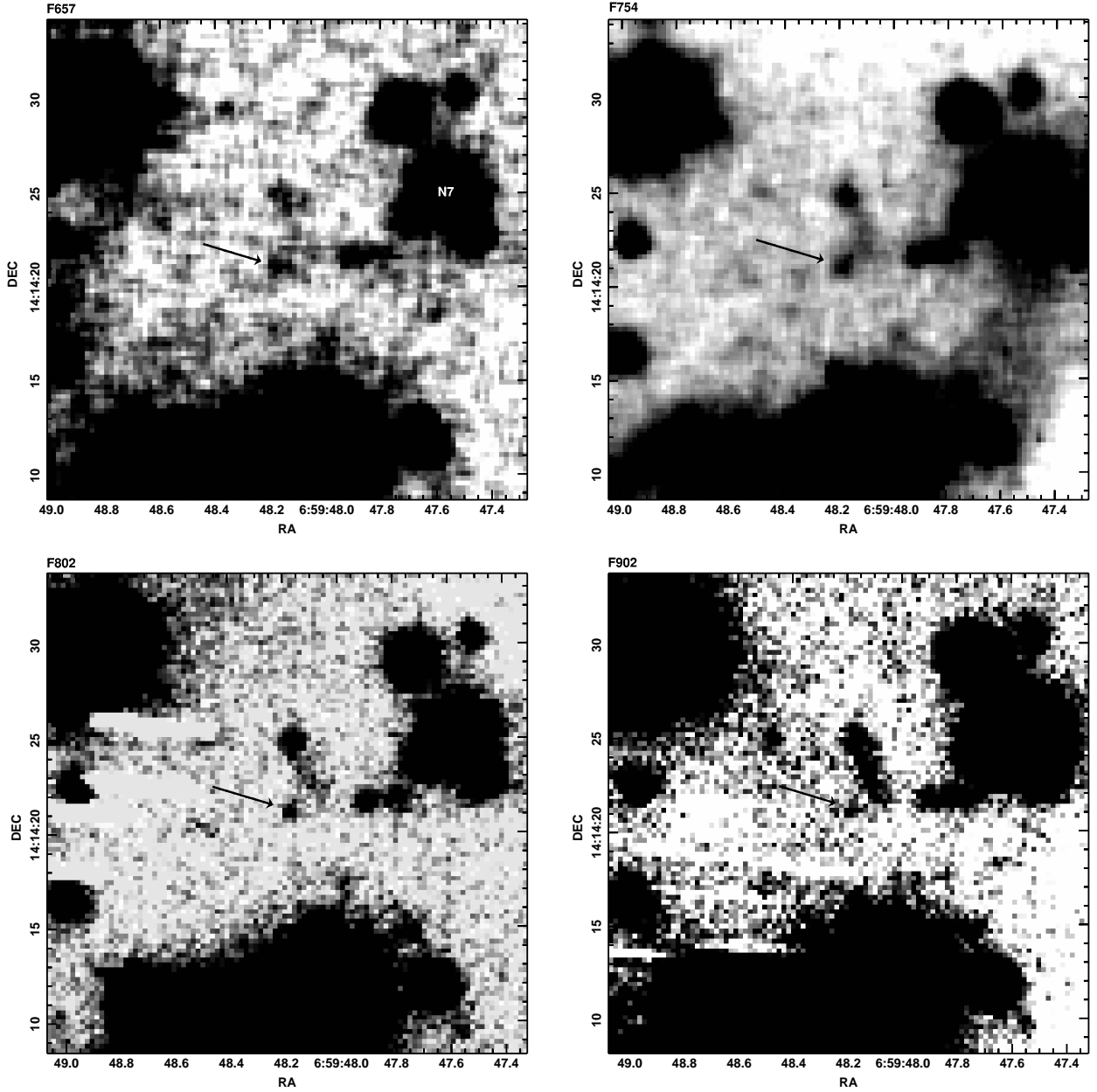


Figure 2. Fragments of the GTC/OSIRIS narrow-band images of the PSR B0656+14 field. The images are smoothed with a three pixel Gaussian kernel. The pulsar optical counterpart is marked by the arrow. The star ‘N7’ from [Koptsevich et al. \(2001\)](#) is marked too in the top-left panel (see discussion below).

four bands. Its instrumental magnitudes were measured in the aperture with a diameter of 4 CCD pixels ($1''.0$) centred at the pulsar position. They were then corrected for the PSF of bright stars and transformed into the resulting pulsar magnitudes. The photometric results are presented in Table 4 and Fig. 7.

2.2 Near-IR broad-band imaging

The observations of the pulsar field were carried out in the J , H , and K_s bands with the Canarias InfraRed Camera Experiment (CIRCE, [Garner et al. \(2014\)](#)) during several runs in 2016 October and November⁹ (see Table 3). CIRCE was operated as a visitor in-

strument equipped with a 2048×2048 engineering grade H2RG detector, which provides a resolution of $0.1 \text{ arcsec pixel}^{-1}$ and a FoV of $3'.4 \times 3'.4$. To properly subtract the rapidly-varying near-IR sky background and reduce the effects of the poor detector cosmetic, we used a self-defined dithering pattern consisting of seven positions. The individual exposures in the H and K_s bands were obtained using the detector Correlated Double Sampling (CDS) mode and were repeated two and three times at each dither position, respectively. The J band observations were performed in the detector Fowler sampling mode, and the individual images were obtained twice at each dither position. The total integration time for the J , H , and K_s bands was 9.24, 4.48 and 3.03 ks.

The CIRCE data were reduced using custom codes written in IDL. All the images were dark subtracted (in particular to account for

⁹ Proposal GTC3-16BIACMEX, PI S. Zharikov

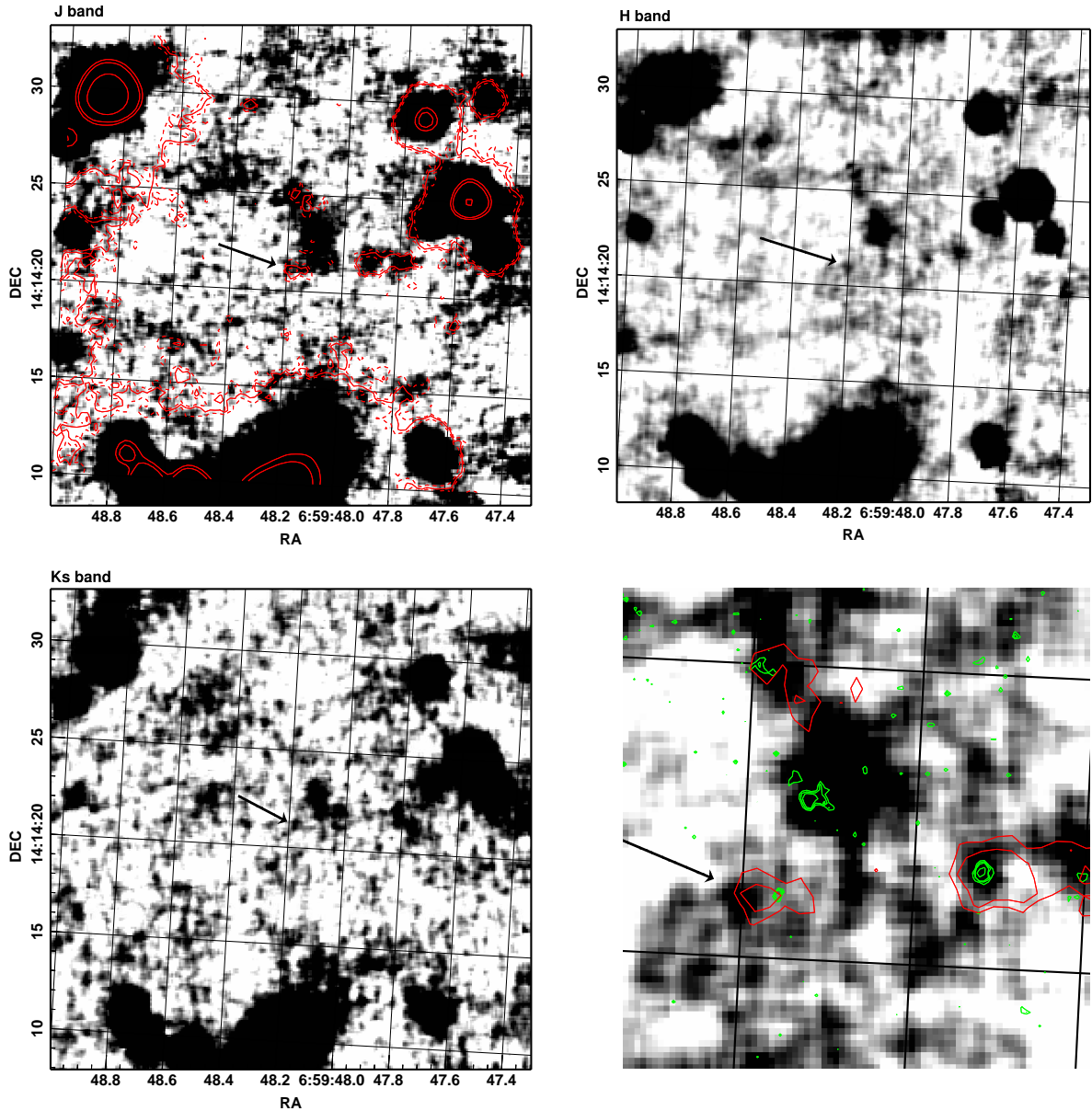


Figure 3. Fragments of the GTC/CIRCE JHK_s images of the PSR B0656+14 field. The $10'' \times 10''$ pulsar vicinity from the H -band image is enlarged in the right bottom panel. All image fragments are smoothed with a three pixel Gaussian kernel. The pulsar counterpart is marked by arrows. The red contours are overlaid from the $F657/35$ band image (see Fig.2) (epoch 2011). The green contours are overlaid from the $HST/FOC F110W$ image (see Koptsevich et al. (2001), Durant et al. (2011)) (epoch 1997). The shift between the positions is due to the pulsar proper motion.

electronic offsets) and flatfielded, where the masterflat was produced as differential flat from a series of bright flats and faint flats. For sky-subtraction, for each image the adjacent image with the closer count-level was used. After performing the primary reduction several bad pixel masks were applied to every individual exposure. This allowed us to fix numerous non-functional pixels, two dead amplifiers and other detector defects. Before combining the individual sky-subtracted images, they were aligned by measuring the centroid of one star in the FoV in all images. A simple mean combination was used to produce the final image. The resulting combined images are shown in Fig. 3. Their astrometric solutions were obtained using a set of seven reference stars in the pulsar vicinity from the *GAIA*

catalogue. The formal rms error of the astrometric calibration was $\approx 0''.02$ in both directions. A set of other stars does not significantly improve the solution.

Inspection of the resulting images showed that the pulsar can be detected at a fair confidence level in the H band and only marginally in the J and K_s bands. The latter is based on the position coincidence of the pulsar and detected counts. To demonstrate this we overlaid the image in the $F657/35$ band by contours on the J band image (Fig. 3, top-left). The more reliable detection of the pulsar in the H band is explained by better seeing conditions during the observations in this band (see Table 3). A small $\sim 0''.2$ dispersion in the pulsar counterpart position in different near-IR bands is visible.

Table 3. Log of the GTC observations of PSR B0656+14.

Date	Band $\lambda/\Delta\lambda$	Exposure $N_{exp} \times [\text{sec}]$	AM sec(Z)	Seeing [arcsec]	Observing conditions
2009-10-17	F657/35	6×250.0	1.18	0.7	Photom.
2009-10-17	F754/50	9×200.0	1.10	0.7	Photom.
2011-10-28	F902/44	2×600.0	1.03	0.7	Photom.
2011-10-28	F902/44	2×300.0	1.04	0.7	Photom.
2011-10-29	F902/44	6×325.0	1.04	0.7	Photom.
2011-10-29	F902/44	6×325.0	1.04	0.7	Photom.
2011-11-21	F902/44	13×325.0	1.03	0.7	Photom.
2011-12-27	F657/35	2×300.0	1.05	0.9	Photom.
2011-12-27	F754/50	2×300.0	1.10	0.9	Photom.
2011-12-27	F802/51	12×300.0	1.12	0.9	Photom.
2012-01-23	F902/44	18×325.0	1.12	0.7	Photom.
2016-10-22	K_s	168×10	1.21	0.8–1.6	Photom.
2016-10-30	J	154×30	1.05	0.8–1.2	Clear
2016-10-31	H	112×20	1.04	0.5–0.8	Clear
2016-11-01	H	112×20	1.04	0.5–0.7	Clear
2016-11-01	J	42×30	1.08	0.5–0.6	Clear
2016-11-08	J	112×30	1.04	0.6–1.1	Clear
2016-11-08	K_s	135×10	1.15	0.6–1.1	Clear

Standards:

OSIRIS: He3 (F657/35, F802/51, F754/50);

OSIRIS: G191-B2B, Feige34, He3 (F902/44);

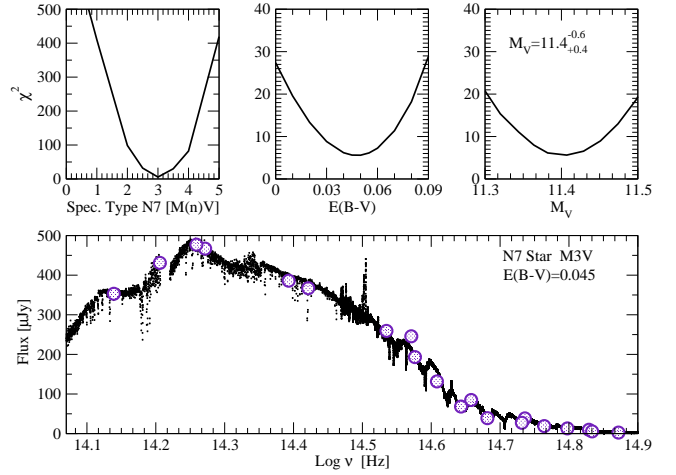
CIRCE: AS05, AS16, AS39

Table 4. GTC photometry of PSR B0656+14.

Band	$\log(\nu)$ [Hz]	Flux _{obs} [μJy]
F657/35	14.659	0.368(32)
F754/50	14.599	0.467(42)
F802/51	14.573	0.356(39)
F902/44	14.522	0.366(61)
J	14.393	0.469(130)
H	14.259	0.639(170)
K_s	14.139	1.059(300)

However, it is a typical situation for objects found near the detection limit ($S/N < 10$) (see, for example, Figure 2 in Zharikov & Mignani (2013)). We also note that the position of the pulsar in the H band perfectly agrees with the expected pulsar radio position calculated for the epoch of the near-IR observations using its proper motion measured in the radio by Briskin et al. (2003). Contours in the bottom-right panel of Fig. 3 demonstrate the proper motion shift with the epoch observed in the optical-near-IR.

The conditions during the GTC/CIRCE observations were clear with slightly (~ 0.1 mag) variable transparency. The photometric calibration was performed based on the standards from the photometric standard fields AS05, AS16 and AS39 from Hunt et al. (1998) observed the same nights as the target. In addition, we used the Two-Micron All-Sky Survey (2MASS) stars (Skrutskie et al. 2006) with a magnitude of $\lesssim 14.5$ and photometric errors $\lesssim 0.05$ mag that fall in the CIRCE FoV. We accounted for the atmospheric extinction using the coefficients 0.09, 0.07 and 0.08 for the J , H , and K_s bands, respectively, provided by the GTC team. As a result, we obtained the photometric zero-points $J^{ZP} = 23.74 \pm 0.03$, $H^{ZP} = 24.20 \pm 0.04$ and $K_s^{ZP} = 23.92 \pm 0.04$.

**Figure 4.** The multi-band *HST*/ACS/WFC, BTA, *HST*/NICMOS and 2MASS photometry (filled circles) of the reference star N7 and its comparison with a template spectrum (points) of the M3V star (from Rayner et al. (2009) and Kesseli et al. (2017)).

We measured the pulsar instrumental magnitudes in the aperture with a diameter of 6 CCD pixels ($0''.6$) centred at the pulsar position computed for the epoch of the near-IR observations. They were corrected for the PSF of bright stars selected in the CIRCE FoV and transformed into the 2MASS JHK_s magnitudes using the obtained zero-points. The magnitudes were then transformed into fluxes using the calibrations from Cohen et al. (2003). The photometric results are presented in Table 4 and Fig. 7.

3 CLARIFICATION OF THE HST/NICMOS NEAR-IR PHOTOMETRY

The *HST*/NICMOS photometry of PSR B0656+14 in the $F110W$, $F160W$ and $F187W$ bands was first reported by Koptsevich et al. (2001) with the respective fluxes 0.336(30), 0.575(30) and 0.779(97) μJy . Durant et al. (2011) have performed independent measurements based on the same data and obtained the fluxes $F110W=0.385(30)$ μJy , $F160W=0.551(30)$ μJy and $F187W=0.660(25)$ μJy . We verified these results using the original data from the *HST* archive and PHOTFNU parameters extracted from the file headers and obtained from the STScI webpage¹⁰. Our measurement of $F160W=0.563(30)$ μJy is in a good consistency with the respective $F160W$ -band flux reported by Koptsevich et al. (2001). The flux in the $F110W$ band equals to 0.340(30) μJy for PHOTFNU=1.84724e-6 (CAMERA2) from the NICMOS webpage and 0.393(30) μJy for PHOTFNU=2.3133694e-6 from the image header. The first value corresponds to the measurement of Koptsevich et al. (2001) and the second one corresponds to that of Durant et al. (2011). We used a sum of all images to estimate the flux in the $F187W$ band. It is important to note that a few cosmic rays were detected close the pulsar position in some images and they significantly complicated the pulsar flux measurements. We verified each image for the presence of cosmic rays at or close to the pulsar position and removed them by interpolating the average background pixel flux in the pulsar vicinity. Our resulting estimation of the pulsar flux in this band, $F187W$

¹⁰ www.stsci.edu/hst/nicmos/performance/photometry/prencs_keywords.html

$=0.668(120) \mu\text{Jy}$, is in agreement with the [Durant et al. \(2011\)](#) measurements, however we note that they underestimated the flux errors. A slight shift (1 pixel) of the photometric aperture centre leads to a significant ($\sim 20\%$) variation of the measured flux.

As was shown above, the mentioned NICMOS calibration uncertainty can lead to the pulsar flux uncertainty above 2σ of statistical errors. To verify the calibration, it is instructive to consider a bright 2MASS reference star located near the pulsar. To do that, [Durant et al. \(2011\)](#) remeasured the fluxes of the object N7 (2MASS J06594760+1414253, see Fig. 2) from [Koptsevich et al. \(2001\)](#) and found them to be about 10% higher than those reported by [Koptsevich et al. \(2001\)](#) and about 20% lower than the 2MASS measurements ($J_{2MASS}=16.37(14)$, $H_{2MASS}=15.56(16)$, $K_{2MASS}=15.13(16)$). In our CIRCE data this object was detected with a high S/N ratio and its magnitudes and colour indices in the 2MASS system are $J=16.54(4)$, $H=15.83(4)$, $K=15.62(4)$, $J-H=0.72(5)$ and $H-K=0.20(4)$. The high precision optical photometry of the object N7 was presented by [Kurt et al. \(1998\)](#) and [Koptsevich et al. \(2001\)](#): $B=22.00(3)$, $V=20.31(2)$, $R_c=19.13(2)$, $I_c=17.74(2)$, $B-V=1.69(4)$, $V-R=1.18(3)$, $R-I=1.38(3)$. The corresponding total Galactic extinction values in the PSR B0656+14 direction are $A_B=0.32$, $A_V=0.24$, $A_R=0.19$, $A_I=0.14$, $A_J=0.06$, $A_H=0.04$ and $A_K=0.03$ ([Schlafly & Finkbeiner 2011](#)). We repeated the *HST/NICMOS* photometry of the N7 object using the individual frames where the object does not fall on the detector edge. The *PHOTFNU* parameters were extracted from the image headers. The measured object fluxes are $F_{110W}^{N7}=320.20(30) \mu\text{Jy}$, $F_{160W}^{N7}=451.32(30) \mu\text{Jy}$ and $F_{187W}^{N7}=351(2) \mu\text{Jy}$.

Taking into account the object magnitudes, colour indices and the total Galactic extinction, we found that the object N7 is likely a M0 – M5 type dwarf star located at a distance of about 750 ± 300 pc ([Hawley et al. 2002](#), [Koen et al. 2002](#)). The *GAIA* parallax¹¹ of the N7 star is $1.88(38)$ mas which corresponds to a distance of 531^{+135}_{-89} pc. The corresponding interstellar extinction for this distance from [Green et al. \(2015, 2018\)](#) yields a colour excess of $E(B-V)=0.02(2)$. To check what fluxes can be expected from the star in the *HST/NICMOS* filters, we calculated them using the M0V-M5V type star IR spectral templates from [Rayner et al. \(2009\)](#). They were extended to the optical range using data from the empirical template library of the Sloan Digital Sky Survey stellar spectra ([Kesseli et al. 2017](#)) using an overlapping region. The best agreement between the observed and calculated colour indices was found for the M3V type star spectra ($M_V = 11.4^{+0.6}_{-0.4}$, $E(B-V)=0.045(20)$), which are consistent within uncertainties with our GTC/CIRCE photometry of the N7 star (see Fig. 4). Using only *JHK_s* data gives reduced chi-square per degree of freedom $\chi^2_{\nu=3} \approx 1$. The optical BTA photometry data (see Section 5.2), after being included in the fit, insignificantly increases the reduced chi-square $\chi^2_{\nu=7} = 5.6$ that is more probably related to band-pass characteristics in the optical range or the star individuality. The narrow band *HST/ACS/WFC* photometry of the N7 star is also in agreement with the N7 star spectral type (the *HST/ACS/WFC* data of the N7 star are presented in Fig. 4).

The best fit shows a full consistency ($\sim 1\%$) between the measured and calculated fluxes in the *F160W* band and a slight discrepancy of $\sim 10\%$ and $\sim 12\%$ for the respective measurements¹² in the *F110W* and *F187W* bands: $F_{110W}^{N7}=353.0 \mu\text{Jy}$, $F_{160W}^{N7}=447.0 \mu\text{Jy}$ and $F_{187W}^{N7}=394.0 \mu\text{Jy}$. We assume that the flux difference

Table 5. Log of the VLT/FORS2 observations of PSR B0656+14.

Date (UT)	Number of exposures	AM	Exposure [s]
2004-11-12	2	1.30	1400
2004-11-14	4	1.30	1400
2004-11-15	2	1.30	1400
2004-11-16	2	1.29	1400
2004-11-17	2	1.29	1400
2004-12-17	4	1.36	1400
2005-02-07	2	1.33	1400

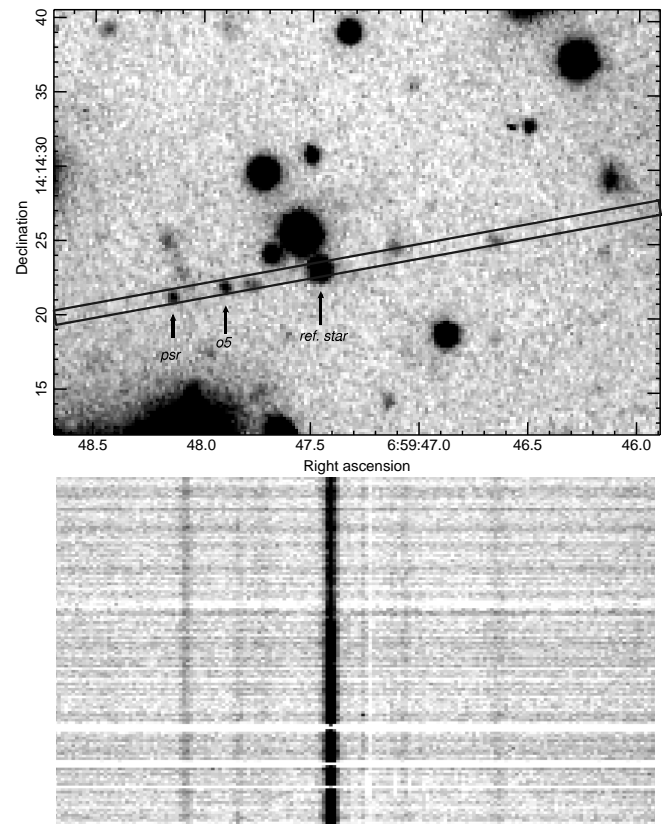


Figure 5. *Top:* R-band image fragment of the pulsar field. The stripe shows the slit and its orientation, which were used to obtain spectra of the pulsar and two nearby stars marked as ‘psr’, ‘o5’ and ‘ref. star’. *Bottom:* fragment of the VLT/FORS2 2D-spectrum of the pulsar and nearby objects in the ‘blue’ optical range.

should be taken into account and that the NICMOS fluxes obtained using *PHOTFNU* from the image header must be corrected accordingly. After applying this correction we obtain the observed pulsar fluxes $F_{110W}=0.432(30) \mu\text{Jy}$, $F_{160W}=0.568(30) \mu\text{Jy}$ and $F_{187W}=0.748(120) \mu\text{Jy}$ (Fig. 7).

¹¹ <https://www.cosmos.esa.int/web/gaia/data-access>

¹² The magnitudes were obtained by convolution of the NICMOS filters transmission curves with the template spectrum and NICMOS zero-points.

Table 6. Log of the *HST*/ACS/WFC observations of PSR B0656+14 and its flux measurements in the Ramp filter sub-bands.

Exp. Time (sec)	$\log(\nu_{C.W.})$ (Hz)	PHOTFLAM (2009) ($\frac{\text{ergs}}{\text{cm}^2 \text{\AA} \text{s}}$)	Flux 2pix (cps)	Flux 3pix (cps)	Flux 4pix (cps)	Flux(2) 0'.5 (cps)	Flux(3) 0'.5 (cps)	Flux(4) 0'.5 (cps)	Flux _{ave} 0'.5 (cps)	Ap. corr. ∞ %	CTE corr. %	Flux _{obs} obs (μJy)	Flux _{obs} derredded (μJy)
1399.8°	14.872(11)*	1.743e-18	0.191	0.255	0.316	0.282	0.307	0.348	0.312(26)	11.7	5.6	0.347	0.387(34)
1020.0°	14.834(11)*	9.520e-19	0.293	0.475	0.629	0.427	0.569	0.69	0.56(10)	9.6	3.6	0.393	0.433(83)
830.0°	14.798(12)*	7.162e-19	0.410	0.472	0.542	0.594	0.565	0.596	0.585(14)	9.1	4.0	0.362	0.396(10)
885.0°	14.764(13)*	5.776e-19	0.412	0.461	0.481	0.591	0.550	0.532	0.557(24)	8.7	3.7	0.323	0.350(15)
1020.0°	14.732(12)*	5.857e-19	0.438	0.483	0.608	0.599	0.568	0.664	0.610(40)	8.4	3.0	0.413	0.443(29)
1020.0°	14.682(11)*	3.779e-19	0.500	0.586	0.610	0.701	0.694	0.672	0.688(11)	8.5	2.5	0.376	0.402(6)
810.0°	14.643(12)*	2.895e-19	0.635	0.732	0.684	0.891	0.864	0.751	0.835(61)	8.3	2.5	0.417	0.442(32)
810.0°	14.608(13)*	2.551e-19	0.499	0.700	0.819	0.790	0.884	0.916	0.863(53)	8.5	2.5	0.447	0.470(29)
747.0°	14.576(14)†	2.427e-19	0.466	0.620	0.697	0.761	0.788	0.785	0.777(11)	8.8	3.2	0.448	0.468(6)
1330.8°	14.535(14)†	2.970e-19	0.325	0.366	0.402	0.623	0.500	0.476	0.533(64)	9.7	2.9	0.457	0.474(57)
2842.0°	14.500(17)†	5.474e-19	0.089	0.098	0.133	0.204	0.153	0.174	0.177(21)	19.8	3.2	0.360	0.372(43)

E(B-V) = 0.03 is selected for flux dereddening; observational epochs: °2005-12-08; °2005-12-03; Ramp filter names: *FR459M; *FR647M; †FR914M
 $\log \nu_{CW}$ - logarithm of frequency corresponding to the filter central wavelength.

Flux(N) is the flux obtained from N pix. aperture by correction to 0'.5 aperture.

$$\text{Flux}_{ave} = \frac{\sum \text{Flux}(N)}{3}$$

Ap. corr. is the correction for the PSF from the 0'.5 aperture to the nominal 'infinite' aperture of 5'.5.

CFE is the charge transfer efficiency.

The final errors include errors of measurements and uncertainties of the interstellar absorption.

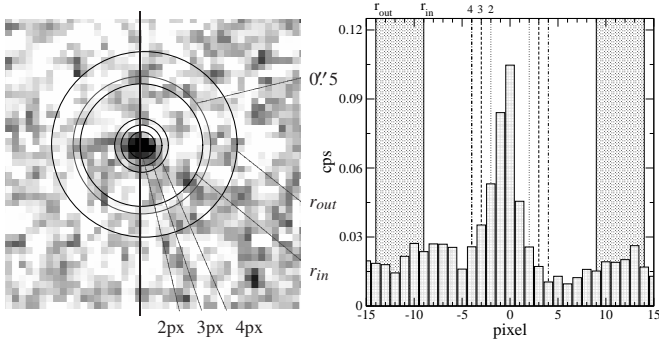


Figure 6. Example of *HST*/ACS/WFC image (left) of the pulsar obtained in the filter FR647M with the central wavelength (CW) corresponding to the frequency $\log \nu_{C.W.} = 14.732$ Hz and the pulsar spatial profile (right). The circular apertures, background region, and the 0'.5 aperture selected for the pulsar photometry are shown in the image. They are also shown by the vertical lines and grey strips in the profile.

4 VLT/FORS2 SPECTROSCOPY

The spectrum of PSR B0656+14 was obtained in 2004 November–December and 2005 February during several observational runs¹³ using the VLT/UT1 telescope in a service mode (see Table 5). The FORS2 instrument was used in a long slit spectroscopic setup with the GRIS_300V grating and the GG435 filter, which cover the wavelength interval of about 4300–9600 Å and provide a medium spectral resolution of 3.35 Å pixel⁻¹. The slit width was 1".0 and its position angle was selected in such a way so it covered several nearby stars for the accurate astrometric referencing and wavelength/flux calibration (see. Fig. 5). Eighteen 1400 s science spectroscopic exposures were taken with a total exposure time of 25.2 ks at a mean seeing of 0".6. Standard reference frames (biases, darks, flatfields, lamps) were

obtained in each observational run, while the slit and slitless observations of the spectrophotometric standards (Feige110, LTT3218 and LTT1788) for the flux calibration were carried out in separate runs during the same nights. A combination of the ESO-MIDAS and IRAF packages was used for standard CCD data reduction, cosmic-ray track removing, spectra extraction and the subsequent data analysis.

PSR B0656+14 is a faint target with $R \approx 24.6$, which is at the limit of the VLT spectroscopic capability. Nevertheless, excellent seeing conditions allowed us to resolve its spectrum even on individual exposures, albeit with a low S/N ratio. The individual exposures were co-added. The spectrum was then extracted with a 3 pixel wide extraction slit (0.2 arcsec pixel⁻¹) centred on the pulsar. The backgrounds were extracted with 6 pixel wide slits centred above and below the centre of the pulsar spectrum. The correction factor for the PSF and sensitivity function were obtained from the Feige110 standard observations. The S/N of the resulting spectrum was about 4 (per pixel) in the 4450–5500 Å range and declined to ~ 1 near/above 8000 Å, due to higher sky backgrounds and a drop in sensitivity towards longer wavelengths. We binned the spectral flux in 20 pixel bins (67Å) to get S/N near/above 15 and 4, respectively, making the flux accuracy to be comparable with that of available photometric data. The resulting optical VLT spectrum of PSR B0656+14 is presented in the top panel of Fig. 7. It is in a good agreement with the photometric data points. In general, it can be described by a single PL, $F_\nu \sim \nu^{-\alpha}$, with a spectral index $\alpha = 0.6(1)$. We found no evidence of any significant narrow (emission or absorption) spectral features. An apparently large spectral variation in the flux density at $\log \nu = 14.55 - 14.65$ Hz is due to the low S/N in this range. Broad weak features could exist in a range of $\log \nu = 14.63 - 14.82$ Hz, however, their significance cannot be claimed confidently.

¹³ ESO program 074.D-0512A, PI R. Mennickent

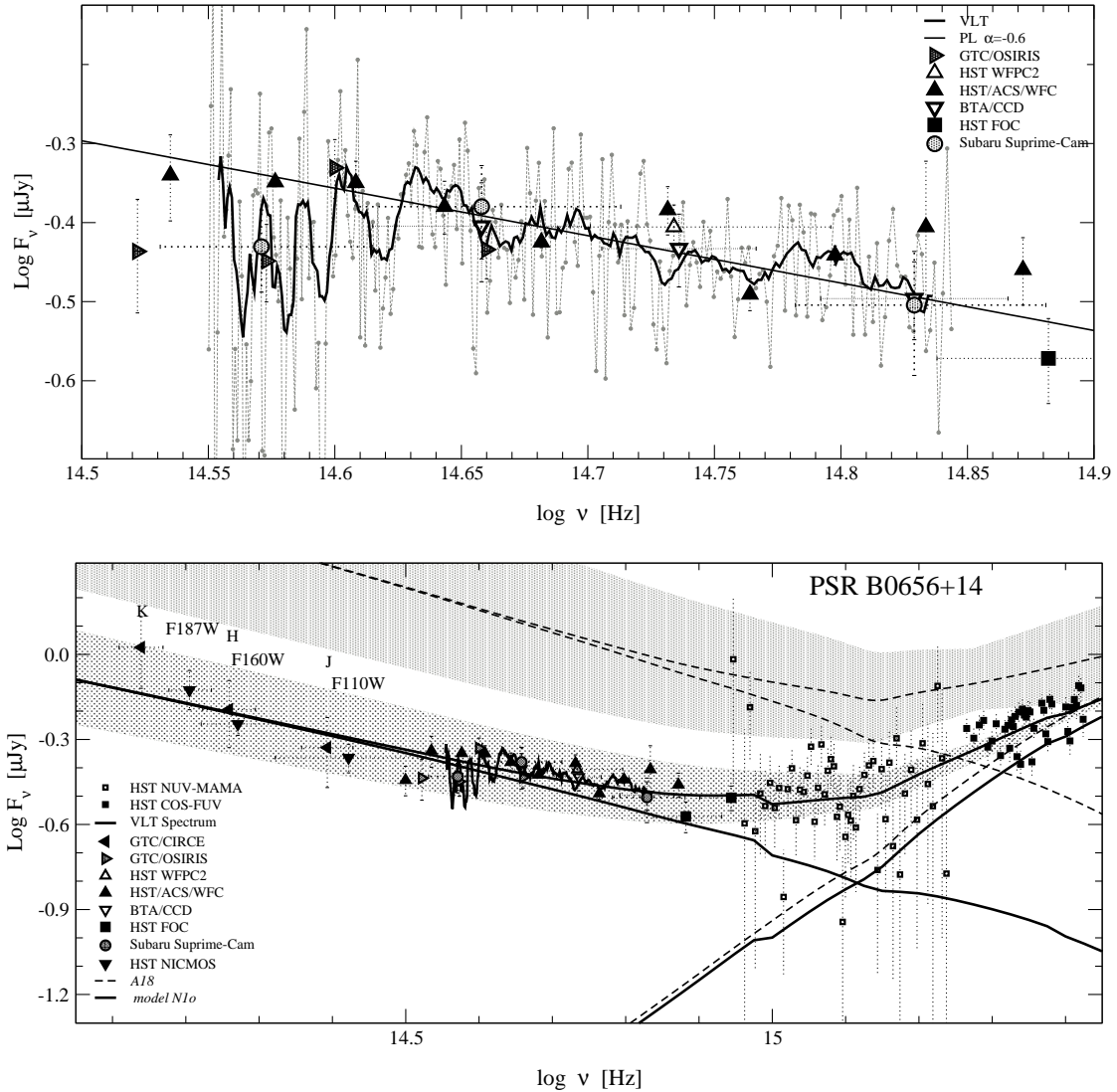


Figure 7. *Top:* observed VLT optical spectrum of PSR B0656+14 shown by the line and broadband photometric points (error-bars) obtained with different telescopes/instruments as notified in the legend. The straight line shows the best fit of the spectrum by the PL model with the spectral index $\alpha \approx 0.6$. *Bottom:* observed UV-optical-near-IR spectrum of the pulsar produced compiling the data from various telescopes discussed in the text. Low-wavelength extrapolations of the absorbed thermal and nonthermal spectral components and their sum obtained from fitting the pulsar X-ray data alone by the G2BB+PL model with the absorption line (Table 7, the fit *N1*). Solid lines show the same when the long-wavelength and X-ray data are fitted together (the fit *N10*). Grey regions show 1σ uncertainties of the fits (see text for details).

5 HST OPTICAL NARROW-BAND PHOTOMETRY AND UV DATA; SUBARU AND BTA BROAD-BAND OPTICAL PHOTOMETRY

5.1 HST/ACS/WFC narrow-band photometry

The *HST/ACS/WFC* observations of the pulsar field were obtained on 2005 December 3 and 12 using the *FR459M*, *FR647M* and *FR914M* filters with 11 central wavelength positions. We extracted the data from the *HST* archive and re-reduced them to consistently compare with the narrow-band GTC photometry and the VLT spectroscopy. This analysis is important as based on these data [Durant et al. \(2011\)](#) reported on the presence of absorption/emission features in the spectrum of the pulsar, while we find no such features in our VLT spectrum. The log of the *HST* observations and results of our photometry are given in Table 6.

We repeated the flux measurements of the pulsar in all available

ACS/WFC bandpasses. For aperture photometry, the circular apertures with radii of 2, 3, and 4 pixels were used (1 pixel = $0''.05$). The aperture centre was chosen by fitting the pulsar profile with a Gaussian in each band (see Fig 6). The background was measured using the annulus with respective inner and outer radii $r_{in} = 9$ and $r_{out} = 14$ pixels for all apertures. Following the *HST/ACS/WFC* user manual¹⁴, the source fluxes measured in count-rates (cps) for each aperture were corrected to an aperture of $0''.5$ using photometry of bright unsaturated nearby star-like objects in the ACS FoV. These corrected fluxes for different initial apertures showed a considerable scattering demonstrating correction uncertainties, which were comparable to statistical count-rate uncertainties. They were then averaged and the final flux errors were derived accounting for

¹⁴ <https://hst-docs.stsci.edu/display/ACSDHB/5.1+Photometry>

the statistical and aperture correction uncertainties. After that, we performed corrections for the PSF from the $0''.5$ aperture to the nominal ‘infinite’ aperture of $5''.5$ and for the charge transfer efficiency (CTE) using the correction factors from [Sirianni et al. \(2005\)](#) and [Chiaberge et al. \(2009\)](#). The fluxes in count-rates were transformed into μJy using PHOTFLAN key-words from image headers. The factors, key-words, and the log of our measurements are given in Table 6. Generally, our results are in agreement with those reported by [Durant et al. \(2011\)](#). Nevertheless, we reduced the scattering of deviations from the power-law fit of the optical spectrum that was visible in previous flux measurements. In addition, we found that the fluxes in the *FR459M* band at $\lambda=4028.805\text{\AA}$ ($\log(\nu_{\text{CW}}) = 14.872$ Hz) and 4400.793\AA ($\log(\nu_{\text{CW}}) = 14.834$ Hz) were slightly overestimated due to the contribution of an extended background structure, likely to be a cosmic-ray track, located at the pulsar position. The revised photometric results are shown in Fig. 7. As seen, they are consistent with the VLT spectroscopy and do not show any significant spectral feature.

5.2 HST UV, BTA and Subaru optical data

The HST UV data on the pulsar were obtained by [Shibanov et al. \(2005\)](#) and [Durant et al. \(2011\)](#) using the STIS NUV-MAMA and COS-FUV instruments, respectively. These data were found to be self-consistent ([Durant et al. 2011](#); see fig.4 therein). We also included in our analysis the published results of the broad-band optical photometry of the pulsar obtained with the Subaru ([Shibanov et al. 2006](#)), and BTA ([Koptsevich et al. 2001](#)) telescopes. These data were obtained by some authors of this study and have been revised and checked independently several times in previous publications. Magnitudes of secondary photometric standards in the pulsar field from [Kurt et al. \(1998\)](#), used for calibration of different sets of optical data, agree with those presented in the Pan-STARRS ([Chambers et al. 2016](#)) and SDSS ([Blanton et al. 2017](#)) catalogues. Therefore, we included in our analysis all these data on the pulsar in their original form. They are also presented in Fig. 7.

6 X-RAY DATA

To perform multi-wavelength analysis of the pulsar spectrum from the near-IR-optical through X-rays, we selected the best-quality published X-ray data sets obtained with *XMM-Newton*, and *NuSTAR* observatories in a photon energy range of 0.15–20 keV (for references see Table 2). We re-reduced the archival X-ray data and extracted time integrated pulsar spectra for fitting them by various models simultaneously with the long wavelength data. Below we briefly describe each of the sets.

The *XMM-Newton* observations were carried out on 2015 September 19 (observation ID 0762890101) and 2019 October 14 (observation ID 0853000201) with total exposure times ≈ 130 ks and ≈ 72 ks, respectively. The latter data set has not been published yet, but it adds a considerable number of source counts to those of the first set, thus allowing one to improve the spectral analysis results. In the observations, the EPIC-MOS cameras were operated in the Timing Mode with the THIN filter setting, and the EPIC-*pn* camera was operated in the Small Window Mode with the THIN filter. The *sas* v.17.0.0 software was used to process the data. In our analysis, we used only the data from the *pn* camera. We selected single and double pixel events ($\text{PATTERN} \leq 4$). Considering light curves we removed periods of background flares. After that, the science

useful *pn* exposures became 84 ks and 71 ks for the first and second sets, respectively. We applied the circular apertures with radii of $37''.5$ and $15''.0$ for energy ranges of 0.15 – 1.4 and 1.4 – 7 keV and extracted the pulsar spectra using EVSELECT tool. The apertures were chosen to increase signal-to-noise of the pulsar spectra (see, e.g. [Arumugasamy et al. \(2018\)](#)). Background was taken from a region free from any sources. We then used *sas* tasks RMFGEN and ARFGEN to generate the redistribution matrix and ancillary response files for the source and background. We analysed the spectra in the 0.3–7 keV range, which is the nominal range for the *pn*. In addition, we checked *pn* spectra in the 0.15–7 keV range, despite the fact that the 0.15–0.3 keV range is not well calibrated¹⁵.

The *NuSTAR* telescope observed the pulsar in 2015 with FPMA and FPMB detectors (observation ID 40101004002). We retrieved the *NuSTAR* data from the archive and reduced them in a similar way as [Arumugasamy et al. \(2018\)](#). *NuSTAR* spectra of the pulsar were analysed in the 3–20 keV range.

7 MULTIWAVELENGTH SPECTRAL ANALYSIS

7.1 Spectral fitting setup

We used the XSPEC v.12.9.0 ([Arnaud 1996](#)) tool for fitting all the data from the near-IR to hard X-rays by theoretical models describing thermal and nonthermal emission of the pulsar. The near-IR–UV data were incorporated into XSPEC using the FTLX2XSP tool ([Blackburn 1995](#)). *XMM-Newton* X-ray spectra were grouped only in the energy range of 1.4 – 7 keV to ensure signal-to-noise of 4 per energy bin and used in our fit simultaneously. The floating cross-normalisation was thawed for each data set while it was fixed at 1 for the *XMM-Newton* data.

For the X-ray photoelectric absorption, we used the XSPEC model TBABS with abundances WILM ([Wilms et al. 2000](#)) and cross-sections BCMC ([Balucinska-Church & McCammon 1992](#)). To account for the interstellar extinction in the optical–UV, we used the XSPEC model REDDEN utilizing the extinction law from [Cardelli et al. \(1989\)](#). Its only parameter, the optical colour excess $E(B - V)$, was linked to the X-ray absorbing column density N_{H} using the relation from [Foight et al. \(2016\)](#), $E(B - V) = N_{\text{H}}/8.9 \times 10^{21} \text{ cm}^{-2}$. The optical transmission REDDEN is set to unity shortward of the Lyman limit, i.e. it does not affect the X-ray data. This is incorrect physically but does allow the model to be used in a combination with the X-ray photoelectric absorption model, which in turn does not directly affect the optical–UV data.

We implemented the fitting by a Markov chain Monte-Carlo (MCMC) sampling procedure assuming a uniform prior distribution for model parameters. We employed the affine-invariant MCMC sampler developed by [Goodman & Weare \(2010\)](#) and implemented in a PYTHON package EMCEE by [Foreman-Mackey et al. \(2013\)](#). About 100 walkers and 15000 steps were typically enough to ensure fit convergences. Using the sampled posterior distribution, we obtained best-fit estimates and credible intervals of the model parameters.

7.2 Spectral fitting results

Following recent X-ray studies (see Sect. 1), we first applied the absorbed G2BB+PL spectral model. It includes 2 BB components

¹⁵ https://xmm-tools.cosmos.esa.int/external/xmm_user_support/documentation/uhb/epicintbkgd.html or <http://xmm2.esac.esa.int/docs/documents/CAL-TN-0018.pdf>

Table 7. Results of the spectral fits of the time integrated emission from PSR B0656+14.

Model	G2BB + PL	G2BB + PL	G2BB + BKPL	G2BB + BKPL	2G2BB + BKPL
spectral range	X-rays in 0.3–20 keV	nIR-opt-UV and X-rays in 0.3–20 keV	nIR-opt-UV and X-rays in 0.3–20 keV	nIR-opt-UV and X-rays in 0.15–20 keV	nIR-opt-UV and X-rays in 0.15–20 keV
fit ID	<i>N1</i>	<i>N1o</i>	<i>N2</i>	<i>N3</i>	<i>N4</i>
Parameter					
N_H (10^{20} cm $^{-2}$)	$4.2^{+1.0}_{-0.9}$	$3.4^{+0.3}_{-0.2}$	$3.1^{+0.4}_{-0.2}$	$2.00^{+0.10}_{-0.10}$	$1.96^{+0.20}_{-0.28}$
$E(B - V)$	$0.047^{+0.011}_{-0.010}$	$0.038^{+0.003}_{-0.002}$	$0.035^{+0.004}_{-0.002}$	$0.022^{+0.001}_{-0.005}$	$0.022^{+0.002}_{-0.003}$
E_c (keV)	$0.53^{+0.02}_{-0.03}$	$0.547^{+0.007}_{-0.006}$	$0.552^{+0.006}_{-0.007}$	$0.570^{+0.006}_{-0.007}$	$0.548^{+0.007}_{-0.008}$
σ (keV)	$0.13^{+0.02}_{-0.03}$	$0.117^{+0.029}_{-0.018}$	$0.110^{+0.019}_{-0.017}$	$0.068^{+0.008}_{-0.010}$	$0.122^{+0.025}_{-0.021}$
s	$0.11^{+0.09}_{-0.06}$	$0.09^{+0.05}_{-0.03}$	$0.076^{+0.038}_{-0.026}$	$0.026^{+0.006}_{-0.05}$	$0.093^{+0.058}_{-0.043}$
$E2_c$ (keV)	-	-	-	-	$0.300^{+0.007}_{-0.018}$
$\sigma2$ (keV)	-	-	-	-	$0.035^{+0.019}_{-0.016}$
$s2$	-	-	-	-	$0.019^{+0.018}_{-0.005}$
$BB1_{norm}$ (10^5)	$2.42^{+1.91}_{-0.82}$	$1.67^{+0.07}_{-0.09}$	$1.52^{+0.11}_{-0.12}$	$1.17^{+0.09}_{-0.10}$	$1.26^{+0.10}_{-0.08}$
R_{BB1} (km)	14^{+5}_{-2}	$11.76^{+0.25}_{-0.43}$	$11.22^{+0.41}_{-0.46}$	$9.87^{+0.37}_{-0.47}$	$10.20^{+0.40}_{-0.32}$
kT_{BB1} (eV)	65^{+3}_{-3}	68^{+1}_{-1}	68^{+1}_{-1}	67^{+1}_{-1}	69^{+2}_{-2}
$BB2_{norm}$	756^{+423}_{-260}	541^{+194}_{-155}	662^{+160}_{-204}	920^{+166}_{-172}	600^{+255}_{-223}
R_{BB2} (km)	$0.80^{+0.20}_{-0.16}$	$0.67^{+0.11}_{-0.11}$	$0.74^{+0.09}_{-0.12}$	$0.87^{+0.08}_{-0.09}$	$0.71^{+0.13}_{-0.14}$
kT_{BB2} (eV)	129^{+6}_{-5}	134^{+6}_{-4}	131^{+6}_{-3}	127^{+3}_{-3}	132^{+6}_{-5}
Γ	$1.79^{+0.13}_{-0.16}$	$1.54^{+0.01}_{-0.01}$	$1.74^{+0.12}_{-0.11}$	$1.82^{+0.13}_{-0.11}$	$1.72^{+0.14}_{-0.09}$
Γ_{opt}	-	Γ	$1.44^{+0.05}_{-0.06}$	$1.35^{+0.06}_{-0.05}$	$1.45^{+0.05}_{-0.06}$
PL_{norm} (10^{-5})	$2.53^{+0.46}_{-0.41}$	$1.97^{+0.11}_{-0.09}$	$3.82^{+1.83}_{-1.15}$	$6.84^{+2.38}_{-2.04}$	$3.47^{+1.60}_{-1.03}$
E_{break} (keV)	-	-	$0.130^{+0.470}_{-0.125}$	$0.120^{+0.201}_{-0.088}$	$0.127^{+0.656}_{-0.101}$
$\ln(Z)$	-307	-390	-380	-445	-394
n	548	620	620	672	672
k	12	12	14	14	17
BIC	690	857	850	981	899

E_c is the Gaussian absorption line central energy, σ and s are its width and strength, respectively. $BB_{norm} = R_{BB}^2/D_{10}^2$ is the blackbody normalisation constant, where D_{10} is the distance to the source in units of 10 kpc (it is fixed at 288 pc), R_{BB} is the radius in km of the BB emitting area, kT_{BB} is the BB temperature. Γ is photon index of the PL component and PL_{norm} is its normalisation in units of photons keV $^{-1}$ cm $^{-2}$ s $^{-1}$ at 1 keV, E_{break} is the energy of the PL spectral break. The errors are given at 90% credible interval. n and k are numbers of data points and varied parameters, respectively. $\ln Z$ is the maximum log-likelihood value and $BIC = k \times \ln(n) - 2 \times \ln(L) +$ is Bayesian information criterion.

describing thermal emission from the bulk of the surface of the cooling NS (BB1) and its hot polar caps (BB2), the PL component from the magnetosphere of the pulsar and the Gaussian absorption line (G;XSPEC model GABS) to account for the X-ray spectral feature reported by [Arumugasamy et al. \(2018\)](#). Using the X-ray data alone we checked that the model provides an acceptable fit to the data in a range of 0.3–20 keV with parameters (Table 7, the fit ID *N1*) generally consistent with those obtained by these authors using only the first *XMM-Newton* data set in the 0.3–7 keV range. Adding the second *XMM-Newton* set and the *NuStar* data results only in a marginal increase of the spectral index of the PL component ($\Gamma = 1.79^{+0.13}_{-0.16}$ vs 1.7 ± 0.1) and the absorbing column density ($N_H = 4.2^{+1.0}_{-0.9}$ cm $^{-2}$ vs $3.0^{+0.7}_{-0.9}$ cm $^{-2}$) and a decrease of the radius of the pulsar ‘hot spot’ ($R_{BB2} \approx 800$ m vs ≈ 1000 m).

Then, we compared the long wavelength extrapolation of the fit *N1* with the observed optical-UV data. This is presented in the lower panel of Fig. 7 where absorbed BB1 and PL contributions and their sum are shown by low, middle and upper dashed lines. The hot BB2 component has a negligible contribution in this range and is not shown. As seen, the extrapolation overshoots the near-IR-optical data by a factor of five. Overshooting the UV data, where the ther-

mal component starts to dominate, is less significant but noticeable (about 1σ). Thus the model with parameters which fit well the X-ray spectrum alone cannot describe the data in the near-IR-optical range.

Therefore, as a next step, we fitted the X-ray and near-IR-optical-UV data simultaneously using the same model. The output of the fit is presented in the Table 7 (the fit ID *N1o*). For the near-IR-optical-UV domain, its results are demonstrated in the lower panel of Fig. 7 where the absorbed BB1 and PL spectral components and their sum are shown by solid lines. The unfolded absorbed best fit model with all its components together with the whole set of the multiwavelength data are presented in the top panel of Fig. 8. According to the fit residuals (the low sub-panel of this plot), the model describes well the data in the whole observing range. Parameters of the thermal components are consistent with those obtained using the X-ray data alone (*N1* fit). However, their uncertainties, as well as the uncertainty of N_H , are much smaller. A significant difference between the two cases demonstrates only the PL component, whose spectrum becomes less steeper when we include the long wavelength data. The photon index of the nonthermal component $\Gamma = 1.54 \pm 0.05$ obtained from the fit *N1o* is consistent with the

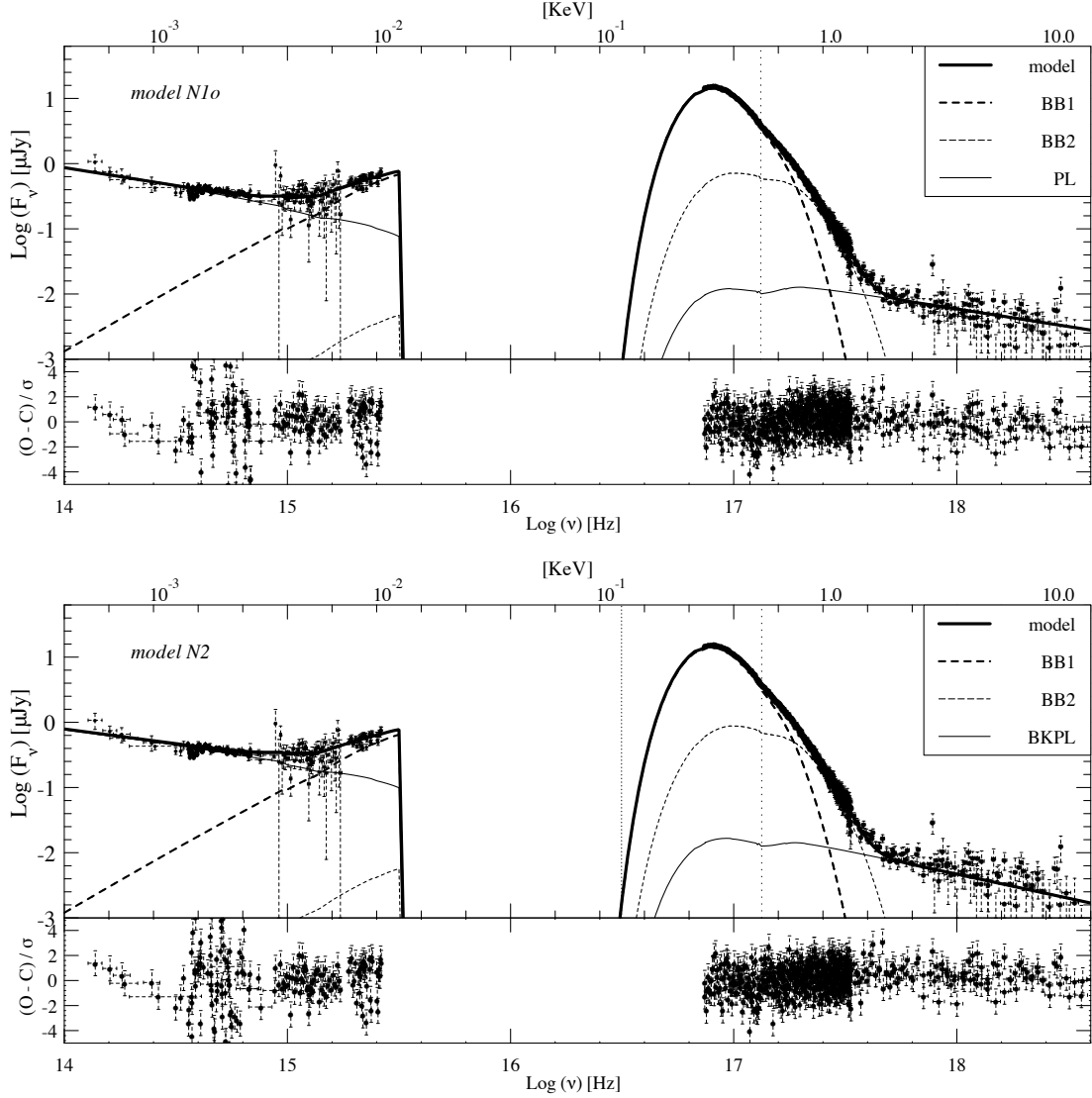


Figure 8. Observed multiwavelength time-integrated spectrum of the pulsar from the IR through X-rays fitted with the absorbed G2BB+PL (*top*) and G2BB+BKPL (*bottom*) models. The VLT optical spectrum is shown without errors to simplify the plot. The best fit models with their components, BB1, BB2, PL/BKPL, are shown by different type lines as notified in legends. The best fit positions of the absorption line and the nonthermal component spectral break (BKPL case) are marked by vertical dotted lines. The fit residuals expressed in terms of the difference between the observed data (O) and the calculated model (C) divided by the data error in each spectral point are shown in the *low sub-panels* of both plots.

spectral index $\alpha = \Gamma - 1 = 0.51 \pm 0.03$ derived from the PL fit of the optical spectrum alone dereddened with the $E(B - V) \approx 0.038$ provided by the *N1o* fit. On the other hand, this component also describes apparently well the nonthermal spectral tail seen in hard X-rays. Although the fit *N1o* is formally acceptable, implying a single PL for the optical and X-ray data, the large difference between the extrapolation of the fit *N1* and the optical-IR data mentioned above indicates that the PL component possibly has a spectral break.

To investigate whether such a break exists in the PSR B0656+14 spectrum and to estimate its parameters, we tried the G2BB+BKPL model, where the BKPL is the broken PL component. The rest of the components are the same as in the previous model. The fit, below referred as *N2*, describes the multiwavelength data almost equally well as the *N1o* fit (Table 7 and the bottom panel of Fig. 8). However, using Bayesian information criteria (BIC; Claeskens & Hjort 2008), we inferred that *N2* has a smaller BIC than *N1o*, making the former

more preferable for the same data sets (see Table 7). Specifically, the obtained $\Delta BIC = 7$ implies *substantial evidence against N1o*. In addition, we evaluated the Bayesian evidence Z (also shown in Table 7) and calculated the Bayesfactor (Goodman 1999a,b) for *N2* over *N1o*, $\Delta \ln Z = \ln(Z_{N2}/Z_{N1o}) = 10$. Assuming equal prior odds for the two models, the posterior odds ratio for the models with the broken power law over the single power law is $Z_{N2}/Z_{N1o} \approx 22000$. This implies that the G2BB+BKPL model is much more probable than the G2BB+PL one, which strongly favours the presence of the spectral break in the nonthermal spectral component of the pulsar. Namely, its spectrum becomes steeper above the break, located at the photon energy between 0.005 – 0.6 keV, with the slope described by $\Gamma = 1.74 \pm 0.12$. The parameters of both thermal components, $E(B - V)$ and N_H remain practically the same as for the fit *N1o*. Ultimately, the G2BB+BKPL model combining thermal emission from the bulk of the surface of the cooling NS, its hot polar caps, and the

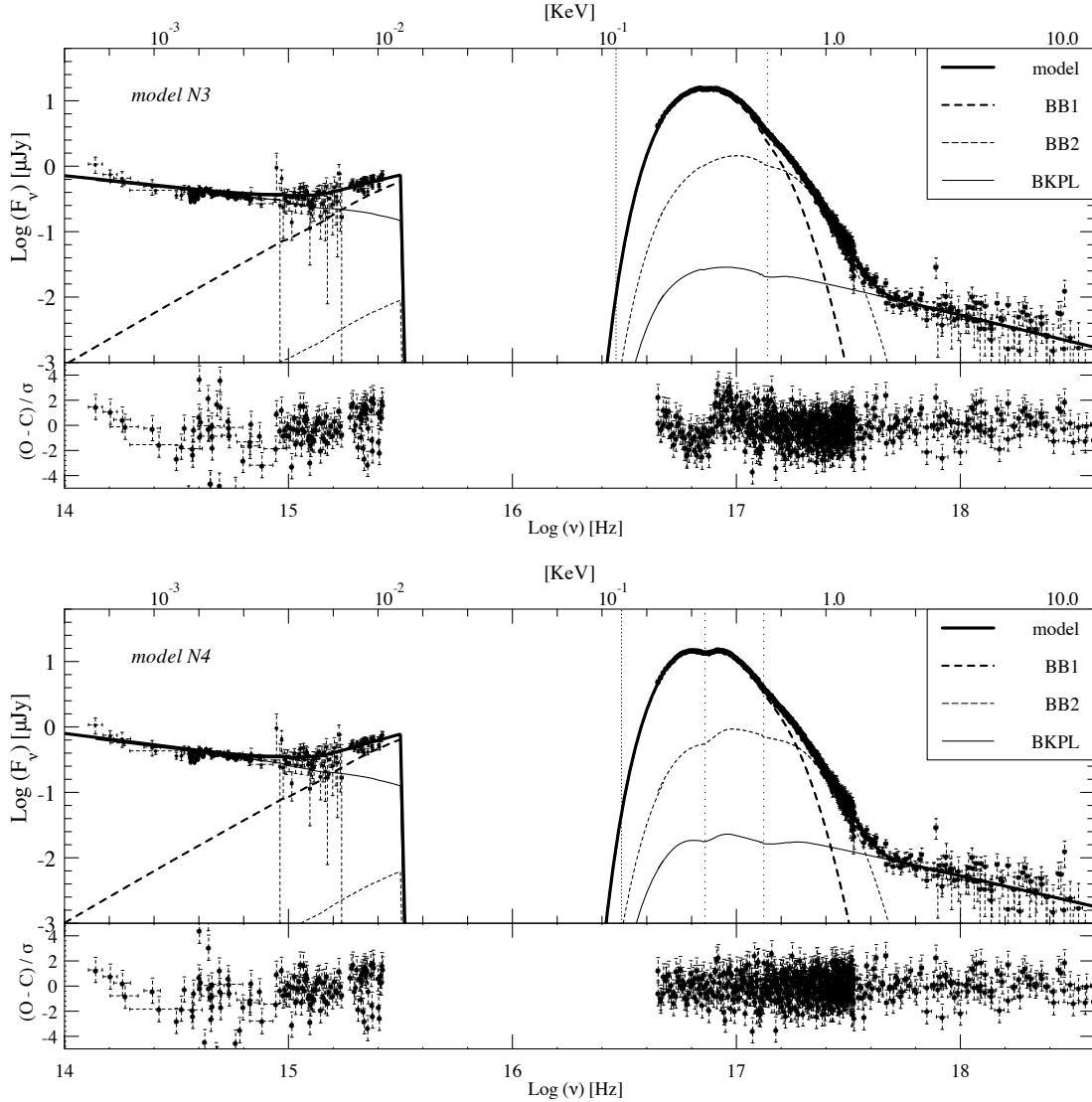


Figure 9. The same as Figure 8 but including the data from the 0.16–0.3 keV range and using the G2BB+BKPL (*top*) and 2G2BB+BKPL (*bottom*) models to fit the spectrum. As seen, the addition of the second Gaussian absorption line into the model excludes prominent fit residuals seen in the soft part of the X-ray spectrum in the *top* panel where the model contains only one Gaussian line.

BKPL emission component of the magnetosphere origin appears to represent the most robust description of the current time-integrated multiwavelength spectrum of the pulsar.

For completeness, we also included the 0.15 – 0.3 keV part of the XMM-Newton/EPIC-pn spectrum of the pulsar so far ignored in the analyses due to possible calibration issues partially related to substantial internal background increase of the pn instrument below 0.3 keV (see Sect. 6). Applying the G2BB+BKPL model to fit the extended data set (the fit ID *N3*) shows characteristic fit residuals in this part of the spectrum indicating a possible presence of a second absorption line (see *top panel* of Figure 9). Indeed, fitting with the 2G2BB+BKPL model, which includes two Gaussian absorption lines, excludes the residuals (*bottom panel* of Figure 9) and allows us to derive the line parameters (the fit ID *N4* in Table 7). It is interesting, that the energy of the second line centre derived from the fit, $E_{2c} \approx 0.3$ keV, is remarkably close to a half of the central energy $E_c \approx 0.6$ keV of the first line, implying that they could represent cyclotron absorption lines created in the magnetised plasma of the

pulsar. The Bayesian evidence and information criteria Z and BIC of the fit *N3* are significantly larger and smaller, respectively, than those in the case the single Gaussian line model (the fit *N3*), formally strongly favoring the presence of the second line. We also note that the interstellar absorption and radius of the cold thermal component become slightly smaller when we include the extended X-ray data set. However, all these issues, including the presence of the second line should be considered with caution. A reliable solution of the EPIC-pn low energy calibration problems and independent detection of the second line with *eROSITA* are required to confirm them.

8 DISCUSSION

Our first spectroscopic, narrow-band optical, and broad-band near-IR observations of PSR B0656+14 with the VLT and the GTC together with the re-analysed archival data obtained with the *HST* and the optical-UV data published since its first identification in the op-

tical about 26 years ago by Caraveo et al. (1994) represent the most reliable and up-to-date complete information on the spectral energy distribution (SED) of the pulsar emission in the near-IR-optical-UV range. The near-IR-optical part of the SED can be described by a single PL with the spectral index $\alpha_\nu \approx 0.6$ (see Fig. 7, top) thus confirming its pulsar magnetosphere origin. The obtained data exclude the presence of any strong narrow spectral lines. There are some hints of weak broad spectral features between 4500Å and 7500Å but their presence can be confirmed only by observations with a higher S/N. Our first observation of the pulsar in the K_s band might allude to the presence of the IR excess over the PL optical SED (see Fig. 7). However, its current significance is only about 1σ . The available *Spitzer* data do not allow us to confirm it due to the strong contamination of the pulsar flux by a distant background galaxy located north-west of the pulsar in its nearest vicinity (see Fig. 3, bottom). High spatial resolution near- and mid-IR observations with large ground-based telescopes equipped by AO systems or with the *JWST* space telescope are necessary to resolve the pulsar from the galaxy. That would be intriguing, as a firm flux increase towards the IR was confirmed so far only for the young PSR B0540–69 (Mignani et al. 2012).

After including two archival data sets obtained with *XMM-Newton* and observations with *NuSTAR* into our X-ray spectral analysis, we confirmed the conclusion of Arumugasamy et al. (2018) based on the single *XMM-Newton* data set on the presence of the absorption line near ≈ 0.6 keV in the time-integrated X-ray spectrum of the pulsar whose X-ray emission in continuum is best described by two blackbody and power-law spectral components. On the other hand, analysing simultaneously the near-IR-optical-UV SED and X-ray data, we conclude that the nonthermal emission component cannot be described by a single power-law in the whole observed range. A flatter near-IR-optical spectrum with photon index $\Gamma_{opt} = 1.44 \pm 0.05$ steepens significantly to $\Gamma_{X-ray} = 1.74^{+0.12}_{-0.11}$ with increasing photon energy towards X-rays suggesting the spectral break between the two ranges. According to our multiwavelength spectral fits the break is presumably located near ≈ 0.1 keV. The presence of spectral breaks in the PL component between the optical and X-rays is typical for most pulsars detected in both spectral ranges (e.g., Shibano et al. 2006, Zharikov et al. 2008, Kirichenko et al. 2014; and references therein) while no multi-wavelength fits have been performed for other pulsars yet.

Including the near-IR-UV SED into the spectral fits together with the X-ray data allows us also to significantly better and self-consistently constrain the parameters of the thermal and nonthermal emission components of the pulsar and the interstellar absorption towards it in the optical and X-rays than it is possible using the data only in separate spectral ranges. For instance, the temperature as measured by a distant observer of the thermal component from the bulk of the surface of the NS, $kT^\infty \approx 68$ eV ($T^\infty \approx 7.9 \times 10^5$ K) is derived from the multiwavelength fit with the accuracy of 1 eV at the 90% credibility level. The latter is a factor of four better than it was obtained by Arumugasamy et al. (2018) using the X-ray data alone. Accounting for the gravitational redshift¹⁶, this yields the NS surface temperature of $\approx 9.6 \times 10^5$ K at $M_{NS} = 1.4M_\odot$ and $R_{NS} = 13$ km. High quality measurements of the effective surface temperatures of isolated cooling NSs are important for comparison with theoretical cooling curves of NSs and obtaining information on still poorly known properties of super-dense matter in their interiors (e.g., Yakovlev & Pethick 2004). Among about fifty NSs whose surface temperatures were estimated mainly based on the X-ray data

(Potekhin et al. 2020a) only for a few stars the temperatures are measured with a high accuracy comparable to that obtained here for PSR B0656+14. Significantly larger temperature errors, at least by a factor of ten, for the rest NSs complicates the data comparison with the theory. As shown here, multiwavelength data can help to considerably decrease the uncertainties and facilitate the progress in this direction.

Based on the most robust G2BB+BKPL model the bolometric thermal luminosity of the bulk of the NS surface is $\log(L_{BB1}^\infty) = 32.54 \pm 0.15$ erg s⁻¹ accounting for the temperature, radius and distance uncertainties. The effective BB radius of the emitting area of the cool thermal component BB1 in the G2BB+BKPL model, $11.22^{+0.41}_{-0.46}$ km, is translated to the circumferential radius¹⁷ of 9.3 ± 0.4 km, accounting for the gravitational light bending near the surface of the NS with $M_{NS} = 1.4M_\odot$ and $R_{NS} = 13$ km. In case if we accept that the emitting region of the BB1 component corresponds to the whole NS surface, the radius of the pulsar becomes unrealistically small, only $R_{NS} = 5.3$ km for $M_{NS} = 1.4M_\odot$, and slightly larger for the smaller pulsar mass.

The fact that the circumferential radius of PSR B0656+14 is smaller than the most plausible NS radius $R_{NS} = 10.7 - 13.1$ km for a neutron star mass of $1.4M_\odot$ (e.g., Lattimer & Prakash 2016, Han & Prakash 2020) shows that the temperature distribution over the NS surface is likely to be non-uniform with a gradient from the magnetic pole to equator, and its surface emission cannot be described by a simple BB model with a single temperature. Such models were considered by Shibano et al. (1995) and Possenti et al. (1996) to explain $\sim 20\%$ pulsed emission fraction in soft X-rays. It is also in accord with the analysis of pulsations of the soft blackbody component and phase resolved X-ray spectroscopy performed by Arumugasamy et al. (2018) showing that R_{BB1} can vary with the pulsar rotation phase from ≈ 6 km to ≈ 22 km in anti-phase to the temperature. Therefore, the radius derived by us from the phase integrated spectra is only an effective radius of radiation from the NS and does not directly correspond to the real physical size of the object.

BB models provide acceptable fits to the thermal components of the spectra of PSR B0656+14, in contrast to NS atmosphere models. This indicates that the observed UV and soft X-ray radiation come from a bare condensed surface of the NS. Indeed, van Adelsberg et al. (2005) showed that the bare condensed surface of a NS produces a spectrum close to a diluted blackbody. Therefore, application of the bare surface model assuming a plausible distribution of the temperature over the surface of the NS and accounting for the pulsar viewing geometry would be the next physically reasonable step in the interpretation of the current and future multiwavelength data of PSR B0656+14. This can provide the most robust constraints on the thermal emission parameters of the NS based on the analyses of the phase resolved spectra and light curves of the pulsar in different spectral bands. R_{NS} and M_{NS} can be also constrained this way as has been recently demonstrated for the isolated millisecond PSR J0030+0451 using *NICER* data (Miller et al. 2019, Riley et al. 2019).

On the other hand, the effective BB radius of the emitting area of the hot thermal component BB2 of about 740 m, is converted to the intrinsic radius of 630 m under the same assumptions. This is about twice as large as the ‘canonical’ polar cap radius of PSR B0656+14, $R_{cp} = R_{NS} \sqrt{2\pi R_{NS}/cP} \approx 360$ m. Therefore, using the BB model with a single temperature for this component should be also consid-

¹⁶ $T = T^\infty / \sqrt{1 - 2.953 M_{NS} (M_\odot) / R_{NS} (km)}$

¹⁷ $R = R^\infty \sqrt{1 - 2.953 M_{NS} (M_\odot) / R_{NS} (km)}$

ered with caution as the simulations predict non-uniform temperature distribution around the polar cap (Harding & Muslimov 2002) with a temperature decreasing towards the outer boundary of the heated region. Multi-wavelength phase resolved spectroscopy and more realistic spectral and light curve models accounting for non-uniform temperature distributions over the entire surface of the NS and its polar caps are needed to further tune the parameters of the pulsar (see previous paragraph).

Other interesting conclusions follow from the assumption that the second X-ray absorption feature near 0.3 keV is real. This and the earlier reported feature at 0.55 keV can represent consequent harmonics of cyclotron absorption in the spectrum of PSR B0656+14. The difference between energies of the lines $\Delta E \approx 0.25$ keV is the cyclotron energy, which allows us to estimate the magnetic field in the region where they could be created: $B_{12} = 0.086(1+z)\Delta E(m/Zm_e)$, where B_{12} is the magnetic field in 10^{12} G units, z is the gravitational redshift $1+z = 1/\sqrt{1-2.953M_{NS}(M_{\odot})/R_{NS}(km)}$, Z and m are the charge and mass of the plasma particle involved into the absorption, and m_e is the electron mass. Assuming electron cyclotron lines ($m = m_e, Z = 1, R_{NS} = 13\text{km}, M_{NS} = 1.4M_{\odot}$), $B_{12} \approx 0.25$, and for the proton lines ($m \approx 1836m_e$), $B_{12} \approx 45.3$. Both values are about twice smaller than those obtained by Arumugasamy et al. (2018) assuming that the 0.55 keV feature is the first cyclotron harmonic. The canonical dipole magnetic field of PSR B0656+14 at the magnetic equator of the NS estimated from the pulsar spin-down, $B_{12} \approx 4.7$, lies between these estimates. This means that the lines are either created in the pulsar magnetosphere or the magnetic field at the NS surface is about 5–10 times stronger and differs from the dipole configuration. The latter situation was observed for several pulsars: PSR J0030+0451 (Bilous et al. 2019, Miller et al. 2019, Riley et al. 2019); PSR J0108-1431 (Arumugasamy & Mitra 2019); PSR J0437-4715 (Lockhart et al. 2019).

9 SUMMARY

Using GTC/OSIRIS and GTC/CIRCE instruments we detected the pulsar B0656+14 in the narrow $F657, F602, F754, F902$ optical bands and in the near-IR JHK_s bands. The displacement of the pulsar counterpart in the data obtained in the last twenty years corresponds to the proper motion that was expected from the Very Long Baseline Array radio observations (Briskin et al. 2003). The narrow-band radiation fluxes of the pulsar are consistent with those measured earlier in broad optical bands. Our K_s data extends, for the first time, the optical-near-IR SED of the pulsar to the $2.2\text{ }\mu\text{m}$ range. We also present a detailed analysis of the first spectral optical observations of the pulsar obtained by us with the VLT. Using the nearest to the pulsar bright field star detected with a high S/N with the GTC and *HST* as a secondary photometric standard, we clarified the near-IR fluxes of the pulsar obtained with the *HST* in the $F110W, F160W$ and $F187W$ broad bands. For the consistency check, we also carefully reanalysed the *HST* optical photometric data obtained with the narrow-band ramp filters $FR459M, FR647M$ and $FR914M$. Combining new results with the broad-band optical data obtained earlier with the *BTA*, Subaru and *HST* telescopes, we find that the observed optical-near-IR SED of the pulsar provided by the spectral and photometric data is well described by a nearly flat power-law with the spectral index $\alpha \approx 0.6$. We do not see any significant narrow spectral features exceeding $\sim 2\sigma$ of standard deviations of the continuum in the pulsar SED. A marginal flux excess over the power-law fit in the $F187W$ and K_s bands is visible suggesting the pulsar flux increase towards the IR, as was indicated by Shibano et al. (2005)

and Durant et al. (2011). Higher quality spectral and photometric data are necessary to confidently confirm the IR excess.

Using the nIR-optical SED, the published UV data obtained with the *HST*, and the best archival X-ray data from *XMM-Newton* and *NuStar*, we performed the self-consistent multi-wavelength spectral analysis of the rotation phase integrated spectrum of the pulsar from the near-IR through hard X-rays until 20 keV. We find that the best spectral fit is provided by the absorbed combined model consisting of the cool black-body emission from the bulk of the surface of the NS, the hot black-body emission from its hot magnetic polar caps, the broken power-law emission of the pulsar magnetosphere origin and the absorption line located near 0.55 keV revealed by Arumugasamy et al. (2018). The temperature of the thermal component from the bulk of the surface of the NS as measured by a distant observer, $kT^{\infty} \approx 68$ eV ($T^{\infty} \approx 7.9 \times 10^5$ K), is derived from the multi-wavelength fit with the accuracy of ≈ 1 eV at the 90% credibility level. The latter is a factor of four better than that obtained using the X-ray data alone. For comparison of this result with NS cooling scenarios see Potekhin et al. (2020b).

The respective circumferential radius of emission region of 9.3 ± 0.4 km is smaller than a typical radius of an NS, $R_{NS} = 13$ km, which suggests nonuniform temperature distribution over the star surface. This is in accord with the results of the rotational phase resolved X-ray spectroscopy by Arumugasamy et al. (2018). The magnetosphere nonthermal spectral component of the pulsar steepens from the optical to X-rays and shows the spectral break likely located near 0.1 keV. Including the poorly calibrated *XMM-Newton* data below 0.3 keV in our spectral analysis reveals a possible presence of the second absorption line in the spectrum of the pulsar near ~ 0.3 keV. Assuming that this line and the 0.55 keV line are formed by cyclotron absorption of the thermal emission from the NS surface, this could be used for direct measurements of the pulsar magnetic field. However, the presence of the 0.3 keV line has to be confirmed by better calibration and *eROSITA* observations.

Our multi-wavelength spectral analysis provides much better constraints on the pulsar parameters than that based on in a single spectral domain. For instance, it gives much more precise and robust location of the pulsar in the $T-N_H$ plane shown in Fig. 1 as compared to previous studies. Black-body fits of the thermal spectral components indicate that this NS is probably covered by a bare condensed matter. Application of the bare NS emission model assuming a plausible distribution of the temperature over the NS surface and accounting for the pulsar viewing geometry would be the next physically reasonable step in the interpretation of the current and future multiwavelength data of PSR B0656+14. This can provide the most robust constraints on the thermal emission parameters of the NS based on the analyses of the phase resolved spectra and light curves in different spectral bands. This will also enable one to measure R_{NS} and M_{NS} and thus put strong constraints on the EoS of super-high density matter in interiors of NSs. The constraints on the pulsar parameters obtained here can be used as initial conditions for such studies.

DATA AVAILABILITY

The data underlying this article will be shared on reasonable request to the corresponding author.

ACKNOWLEDGEMENTS

We are grateful to the anonymous referee for the valuable comments which helped to improve this paper. The manuscript is based on observations made with the Gran Telescopio Canarias (GTC), installed in the Spanish Observatorio del Roque de los Muchachos of the Instituto de Astrofísica de Canarias, in the island of La Palma. Development of CIRCE was supported by the University of Florida and the National Science Foundation (grant AST-0352664), in collaboration with IUCAA. IRAF is distributed by the National Optical Astronomy Observatory, which is operated by the Association of Universities for Research in Astronomy (AURA) under a cooperative agreement with the National Science Foundation. This research has made use of the USNOFS Image and Catalogue Archive operated by the United States Naval Observatory, Flagstaff Station (<http://www.nofs.navy.mil/data/fchpix/>). This publication makes use of data products from the Two Micron All Sky Survey, which is a joint project of the University of Massachusetts and the Infrared Processing and Analysis Center/California Institute of Technology, funded by the National Aeronautics and Space Administration and the National Science Foundation. Some/all of the data presented in this paper were obtained from the Mikulski Archive for Space Telescopes (MAST). STScI is operated by the Association of Universities for Research in Astronomy, Inc., under NASA contract NAS5-26555. DAZ thanks Pirinem School of Theoretical Physics for hospitality. R.E.M. gratefully acknowledges support by FONDECYT 1190621, and the Chilean Centro de Excelencia en Astrofísica y Tecnologías Afines (CATA) BASAL grant AFB-170002. SZ acknowledges PAPIIT grant IN102120.

REFERENCES

- Abdo A. A., et al., 2013, *ApJS*, **208**, 17
- Abdollahi S., et al., 2020, *ApJS*, **247**, 33
- Anderson S. B., Cordova F. A., Pavlov G. G., Robinson C. R., Thompson Jr. R. J., 1993, *ApJ*, **414**, 867
- Arnaud K. A., 1996, in Jacoby G. H., Barnes J., eds, *Astronomical Society of the Pacific Conference Series Vol. 101, Astronomical Data Analysis Software and Systems V* p. 17
- Arumugasamy P., Mitra D., 2019, *MNRAS*, **489**, 4589
- Arumugasamy P., Kargaltsev O., Posselt B., Pavlov G. G., Hare J., 2018, *ApJ*, **869**, 97
- Balucinska-Church M., McCammon D., 1992, *ApJ*, **400**, 699
- Beskin G. M., Neustroev V. V., 2001, *A&A*, **374**, 584
- Beznogov M. V., Yakovlev D. G., 2015, *MNRAS*, **447**, 1598
- Bilous A. V., et al., 2019, *ApJ*, **887**, L23
- Birzan L., Pavlov G. G., Kargaltsev O., 2016, *ApJ*, **817**, 129
- Blackburn J. K., 1995, *FTOOLS: A FITS Data Processing and Analysis Software Package*. p. 367
- Blanton M. R., et al., 2017, *AJ*, **154**, 28
- Briskin W. F., Thorsett S. E., Golden A., Goss W. M., 2003, *ApJ*, **593**, L89
- Caraveo P. A., Bignami G. F., Mereghetti S., 1994, *ApJ*, **422**, L87
- Cardelli J. A., Clayton G. C., Mathis J. S., 1989, *ApJ*, **345**, 245
- Chambers K. C., et al., 2016, arXiv e-prints, p. [arXiv:1612.05560](https://arxiv.org/abs/1612.05560)
- Chiaberge M., Lim P. L., Kozhurina-Platais V., Sirianni M., Mack J., 2009, Technical report, Updated CTE photometric correction for WFC and HRC
- Claeskens G., Hjort N. L., 2008, *Model Selection and Model Averaging*. Cambridge Series in Statistical and Probabilistic Mathematics, Cambridge University Press, doi:10.1017/CBO9780511790485
- Cocke W. J., Disney M. J., Taylor D. J., 1969, *Nature*, **221**, 525
- Cohen M., Wheaton W. A., Megeath S. T., 2003, *AJ*, **126**, 1090
- Cordova F. A., Middleditch J., Hjellming R. M., Mason K. O., 1989, *ApJ*, **345**, 451
- De Luca A., Caraveo P. A., Mereghetti S., Negroni M., Bignami G. F., 2005, *ApJ*, **623**, 1051
- Durant M., Kargaltsev O., Pavlov G. G., 2011, *ApJ*, **743**, 38
- Edelstein J., Seon K.-I., Golden A., Min K.-W., 2000, *ApJ*, **539**, 902
- Finley J. P., Ogelman H., Kiziloglu U., 1992, *ApJ*, **394**, L21
- Foight D. R., Güver T., Özel F., Slane P. O., 2016, *ApJ*, **826**, 66
- Foreman-Mackey D., Hogg D. W., Lang D., Goodman J., 2013, *PASP*, **125**, 306
- Gaia Collaboration et al., 2016, *A&A*, **595**, A1
- Gaia Collaboration et al., 2018, *A&A*, **616**, A1
- Garner A., et al., 2014, in Ramsay S. K., McLean I. S., Takami H., eds, *Proc. SPIE Conf. Ser. Vol. 9147, Ground-Based and Airborne Instrumentation for Astronomy V* SPIE, Bellingham, p. 91474A.
- Goodman S. N., 1999a, *Ann Intern Med.*, **130**, 995
- Goodman S. N., 1999b, *Ann Intern Med.*, **130**, 1005
- Goodman J., Weare J., 2010, *COMM APP MATH COM SC*, **5**, 65
- Gould D. M., Lyne A. G., 1998, *MNRAS*, **301**, 235
- Green G. M., et al., 2015, *ApJ*, **810**, 25
- Green G. M., et al., 2018, preprint, ([arXiv:1801.03555](https://arxiv.org/abs/1801.03555))
- Greiveldinger C., et al., 1996, *ApJ*, **465**, L35
- Han S., Prakash M., 2020, *ApJ*, **899**, 164
- Harding A. K., Muslimov A. G., 2002, *ApJ*, **568**, 862
- Hawley S. L., et al., 2002, *AJ*, **123**, 3409
- Hill R. J., Dolan J. F., Bless R. C., Boyd P. T., Percival J. W., Taylor M. J., van Citters G. W., 1997, *ApJ*, **486**, L99
- Ho W. C. G., 2014, in Petit P., Jardine M., Spruit H. C., eds, *IAU Symposium Vol. 302, Magnetic Fields throughout Stellar Evolution*. pp 435–438 ([arXiv:1311.5583](https://arxiv.org/abs/1311.5583)), doi:10.1017/S1743921314002683
- Hunt L. K., Mannucci F., Testi L., Migliorini S., Stanga R. M., Baffa C., Lisi F., Vanzì L., 1998, *AJ*, **115**, 2594
- Kern B., Martin C., Mazin B., Halpern J. P., 2003, *ApJ*, **597**, 1049
- Kesseli A. Y., West A. A., Veyette M., Harrison B., Feldman D., Bochanski J. J., 2017, *ApJS*, **230**, 16
- Kirichenko A., Danilenko A., Shibanov Y., Shternin P., Zharikov S., Zyuzin D., 2014, *A&A*, **564**, A81
- Koen C., Kilkenny D., van Wyk F., Cooper D., Marang F., 2002, *MNRAS*, **334**, 20
- Koptsevich A. B., Pavlov G. G., Zharikov S. V., Sokolov V. V., Shibanov Y. A., Kurt V. G., 2001, *A&A*, **370**, 1004
- Kurt V. G., Komberg B. V., Sokolov V. V., Zharykov S. V., 1997, *Ap&SS*, **252**, 451
- Kurt V. G., Sokolov V. V., Zharikov S. V., Pavlov G. G., Komberg B. V., 1998, *A&A*, **333**, 547
- Kuzmin A. D., Ershov A. A., 2006, *Astronomy Letters*, **32**, 583
- Lattimer J. M., Prakash M., 2016, *Phys. Rep.*, **621**, 127
- Liszt H., 2014, *ApJ*, **780**, 10
- Lloyd D. A., Perna R., Slane P., Nicastro F., Hernquist L., 2003, *ArXiv Astrophysics e-prints*, astro-ph/0306235.
- Lockhart W., Gralla S. E., Özel F., Psaltis D., 2019, *MNRAS*, **490**, 1774
- Lorimer D. R., Yates J. A., Lyne A. G., Gould D. M., 1995, *MNRAS*, **273**, 411
- Manchester R. N., Lyne A. G., Taylor J. H., Durdin J. M., Large M. I., Little A. G., 1978, *MNRAS*, **185**, 409
- Manchester R. N., Hobbs G. B., Teoh A., Hobbs M., 2005, *AJ*, **129**, 1993
- Marshall H. L., Schulz N. S., 2002, *ApJ*, **574**, 377
- Martin C., Halpern J. P., Schiminovich D., 1998, *ApJ*, **494**, L211
- Massey P., Strobel K., Barnes J. V., Anderson E., 1988, *ApJ*, **328**, 315
- Mignani R. P., 2011, *Advances in Space Research*, **47**, 1281
- Mignani R. P., De Luca A., Caraveo P. A., 2000, *ApJ*, **543**, 318
- Mignani R. P., Zharikov S., Caraveo P. A., 2007, *A&A*, **473**, 891
- Mignani R. P., De Luca A., Hummel W., Zajczyk A., Rudak B., Kanbach G., Słowikowska A., 2012, *A&A*, **544**, A100
- Mignani R. P., Moran P., Shearer A., Testa V., Słowikowska A., Rudak B., Krzeszowski K., Kanbach G., 2015, *A&A*, **583**, A105
- Mignani R. P., et al., 2016, *ApJ*, **825**, 151
- Mignani R. P., Testa V., Rea N., Marelli M., Salvetti D., Torres D. F., De Oña Wilhelmi E., 2018, *MNRAS*,
- Mignani R. P., et al., 2019, *ApJ*, **871**, 246

- Miller M. C., et al., 2019, *ApJ*, **887**, L24
- Mineo T., Massaro E., Cusumano G., Becker W., 2002, *A&A*, **392**, 181
- Nasuti F. P., Mignani R., Caraveo P. A., Bignami G. F., 1996, *A&A*, **314**, 849
- Nousek J. A., Cowie L. L., Hu E., Lindblad C. J., Garmire G. P., 1981, *ApJ*, **248**, 152
- Oke J. B., 1974, *ApJS*, **27**, 21
- Oke J. B., 1990, *AJ*, **99**, 1621
- Pavlov G. G., Stringfellow G. S., Cordova F. A., 1996, *ApJ*, **467**, 370
- Pavlov G. G., Zavlin V. E., Sanwal D., 2002, in Becker W., Lesch H., Trümper J., eds, *Neutron Stars, Pulsars, and Supernova Remnants*. p. 273 ([arXiv:astro-ph/0206024](https://arxiv.org/abs/astro-ph/0206024))
- Possenti A., Mereghetti S., Colpi M., 1996, *A&A*, **313**, 565
- Potekhin A. Y., Zyuzin D. A., Yakovlev D. G., Beznogov M. V., Shibano Y. A., 2020a, *MNRAS*, **496**, 5052
- Potekhin A. Y., Zyuzin D. A., Yakovlev D. G., Beznogov M. V., Shibano Y. A., 2020b, *MNRAS*, **496**, 5052
- Ramanamurthy P. V., Fichtel C. E., Kniffen D. A., Sreekumar P., Thompson D. J., 1996, *ApJ*, **458**, 755
- Rangelov B., Pavlov G. G., Kargaltsev O., Reisenegger A., Guillot S., van Kerkwijk M. H., Reyes C., 2017, *ApJ*, **835**, 264
- Rayner J. T., Cushing M. C., Vacca W. D., 2009, *ApJS*, **185**, 289
- Riley T. E., et al., 2019, *ApJ*, **887**, L21
- Sandberg A., Sollerman J., 2009, *A&A*, **504**, 525
- Schlaflly E. F., Finkbeiner D. P., 2011, *ApJ*, **737**, 103
- Schlegel D. J., Finkbeiner D. P., Davis M., 1998, *ApJ*, **500**, 525
- Schwope A., G. L., Traulsen I., Maitra I., M. R., eSASS team 2019, Report, The eROSITA observation of the isolated neutron star pulsar B0656+14. MPE/IK
- Serafimovich N. I., Shibano Y. A., Lundqvist P., Sollerman J., 2004, *A&A*, **425**, 1041
- Shearer A., et al., 1997, *ApJ*, **487**, L181
- Shibano Y. A., Pavlov G. G., Zavlin V. E., Qin L., Tsuruta S., 1995, in Böhringer H., Morfill G. E., Trümper J. E., eds, Vol. 759, *Seventeenth Texas Symposium on Relativistic Astrophysics and Cosmology*. p. 291, [doi:10.1111/j.1749-6632.1995.tb17547.x](https://doi.org/10.1111/j.1749-6632.1995.tb17547.x)
- Shibano Y. A., Sollerman J., Lundqvist P., Gull T., Lindler D., 2005, *A&A*, **440**, 693
- Shibano Y. A., et al., 2006, *A&A*, **448**, 313
- Sirianni M., et al., 2005, *PASP*, **117**, 1049
- Skrutskie M. F., et al., 2006, *AJ*, **131**, 1163
- Sollerman J., Lundqvist P., Lindler D., Chevalier R. A., Fransson C., Gull T. R., Pun C. S. J., Sonneborn G., 2000, *ApJ*, **537**, 861
- Stone R. P. S., 1977, *ApJ*, **218**, 767
- Tao G.-C., Esamdin A., Hu H.-D., Qian M.-F., Li J., Wang N., 2012, *Research in Astronomy and Astrophysics*, **12**, 1649
- Taylor J. H., Manchester R. N., Lyne A. G., 1993, *ApJS*, **88**, 529
- Thorsett S. E., Benjamin R. A., Briske W. F., Golden A., Goss W. M., 2003, *ApJ*, **592**, L71
- Weltevrede P., Stappers B. W., Rankin J. M., Wright G. A. E., 2006, *ApJ*, **645**, L149
- Wilms J., Allen A., McCray R., 2000, *ApJ*, **542**, 914
- Yakovlev D. G., Pethick C. J., 2004, *ARA&A*, **42**, 169
- Zavlin V. E., Pavlov G. G., 2004, *Mem. Soc. Astron. Italiana*, **75**, 458
- Zavlin V. E., Pavlov G. G., Shibano Y. A., 1996, *A&A*, **315**, 141
- Zharikov S., Mignani R. P., 2013, *MNRAS*, **435**, 2227
- Zharikov S., Mennickent R. E., Shibano Y., Komarova V., 2007, *Ap&SS*, **308**, 545
- Zharikov S. V., Shibano Y. A., Zyuzin D. A., Mennickent R. E., Komarova V. N., 2008, *A&A*, **492**, 805
- Zyuzin D., Shibano Y., Danilenko A., Mennickent R. E., Zharikov S., 2013, *ApJ*, **775**, 101
- Zyuzin D., Zharikov S., Shibano Y., Danilenko A., Mennickent R. E., Kirichenko A., 2016, *MNRAS*, **455**, 1746
- van Adelsberg M., Lai D., Potekhin A. Y., Arras P., 2005, *ApJ*, **628**, 902
- van Kerkwijk M. H., Kulkarni S. R., 2001, *A&A*, **378**, 986

This paper has been typeset from a \LaTeX file prepared by the author.